

Good Graph to Optimize: Cost-Effective, Budget-Aware Bundle Adjustment in Visual SLAM

Yipu Zhao, *Member, IEEE*, Justin S. Smith, *Student Member, IEEE*, Patricio A. Vela, *Member, IEEE*,

Abstract—The cost-efficiency of visual(-inertial) SLAM (VSLAM) is a critical characteristic of resource-limited applications. While hardware and algorithm advances have been significantly improved the cost-efficiency of VSLAM front-ends, the cost-efficiency of VSLAM back-ends remains a bottleneck. This paper describes a novel, rigorous method to improve the cost-efficiency of local BA in a BA-based VSLAM back-end. An efficient algorithm, called *Good Graph*, is developed to select size-reduced graphs optimized in local BA with condition preservation. To better suit BA-based VSLAM back-ends, the *Good Graph* predicts future estimation needs, dynamically assigns an appropriate size budget, and selects a condition-maximized subgraph for BA estimation. Evaluations are conducted on two scenarios: 1) VSLAM as standalone process, and 2) VSLAM as part of closed-loop navigation system. Results from the first scenario show *Good Graph* improves accuracy and robustness of VSLAM estimation, when computational limits exist. Results from the second scenario, indicate that *Good Graph* benefits the trajectory tracking performance of VSLAM-based closed-loop navigation systems, which is a primary application of VSLAM.

Index Terms—visual odometry (VO), visual simultaneous localization and mapping (VSLAM), mapping

I. INTRODUCTION

Visual(-inertial) simultaneous localization and mapping (VSLAM) has applications in robotics and augmented reality (AR) that span a diverse range of platforms. Consequently, the computational resources of robotics and AR implementations are equally variable. For instance, a micro flying vehicle requires lightweight computing kits, and an AR headset typically has an ARM-based System-On-Chip (SoC) with low power consumption. At the other extreme, autonomous vehicles have more room and power for compute hardware. Though many state-of-the-art VSLAM systems achieve real-time performance on a PC or a laptop with a powerful CPU, there may be underlying processes hampered by the sequencing or timing of the pipeline [1]. Some VSLAM systems fail to achieve real-time processing when subject to computational or time limits [2]. Others prioritize efficiency but exhibit performance loss [3], [4]. The impacts and trade-offs magnify when attempting to replicate the same level of performance on less powerful devices [5]. For practical robotics and AR applications, the cost-efficiency of VSLAM is essential and needs improvement.

Y. Zhao is with Facebook Reality Lab (FRL). This work was done when Y. Zhao was with the School of Electrical and Computer Engineering, Georgia Institute of Technology. J. S. Smith and P. A. Vela are with the School of Electrical and Computer Engineering, and Institute of Robotics and Intelligent Machines, Georgia Institute of Technology. E-mails: yipu.zhao@gatech.edu, jssmith@gatech.edu, pvela@gatech.edu.

This research was funded in part by the National Science Foundation (Award #1816138).

Efficient VSLAM front-ends, that is, visual feature tracking, has been pursued from both hardware and algorithmic perspectives. Dedicated processing units such as FPGAs [6], [7] and GPUs [8] accelerate the highly parallelizable feature extraction step. Meanwhile, better algorithm designs, such as the incorporation of active feature matching [9], improve front-end runtime properties. While this progress enable cost-effective VSLAM front-ends, the cost-efficiency of the VSLAM back-end, that is, state optimization, continues to be a bottleneck. Bundle Adjustment (BA) has been recognized as the favored back-end solution; it estimates both camera poses and maps with high accuracy and robustness. However, BA is computationally expensive: it optimizes a large number of states with up to cubic complexity, and the computation process is largely iterative.

As with the front-end, recognizing the need to improve BA compute time has led to parallel implementations of BA solving on multi-core CPUs [10] and GPUs [11], [12]. These parallel BA methods address the time-sensitive nature of the BA problem (especially for large-scale problems), but they don't fully reduce the compute and power requirement in BA solving. For both compute and power limited configurations frequently seen in robotics and AR platforms, specialized hardware such as FPGAs may serve as co-compute components to speed up specific steps in the BA computations (e.g., FPGA-based Schur elimination [13]). However the remaining BA steps that don't translate to hardware, such as re-linearization and factorization, limit the possible compute reductions of BA-based back-ends. Another hardware platform is the graph processor [14], which shows great potential over conventional CPU-based BA solving. Joint hardware and software acceleration strategies will most likely provide the best approach to accurate and cost-effective VSLAM back-end BA solutions.

Algorithm improvements typically seek to replace or reduce the scale of BA problem in VSLAM system. Some state-of-the-art VSLAM systems [4], [15] choose less expensive filters over BA as the back-end solution. The computational complexity of filters such as MSCKF [16] is linear in the cardinality of map states. However, these filters have the downside of inconsistency and degraded mapping [17]. The majority of state-of-the-art VSLAM systems utilize BA-based back-ends to achieve high performance. To reduce of the cost of BA, state optimization is typically separated into two semi-independent parts: a high-rate, scale-limited optimization (local BA) and a low-rate full optimization (global BA). The cost-efficiency of a BA-based back-end is largely determined by the high-rate local BA. Several strategies exist to identify scale-limited states for the local BA problem. Many systems [3], [18]–[22]

only keep recent states (e.g. camera frames and map points) that stay within a sliding-window. Other systems [23]–[26] use the covisibility graph to organize historical states and query the covisible subgraph for local BA construction. However, the heuristic strategies described above do not provide insight into the conditioning of the local BA problem. In the presence of computational limits, the small subset of states selected with these heuristic strategies could form an ill-conditioned local BA that is either slow to converge or degrades solution accuracy.

In this paper, we propose a novel, rigorous method to determine the state subset in local BA, called *Good Graph*, with optimization performance guarantees. Inspired by recent progress in submodular submatrix selection [27], [28], we describe an efficient algorithm for selecting a subset of states to define a scale-limited local BA problem that maximizes its conditioning relative to the full BA problem (Section IV). We also describe SLAM specific modifications attuned to the needs of local BA in the back-end (Section V). In particular, given that local BA size and compute time are related, we propose to determine the size of the desired *Good Graph* for local BA by predicting, on-the-fly, the available optimization time budget to best support pose estimation in the near future. A small *Good Graph* is selected for the local BA optimization when the time budget is small (e.g. due to fast motion, or limited computational resources). Otherwise, a large *Good Graph* is selected because the time budget can afford it.

The proposed *Good Graph* algorithm is a form of active problem selection for the BA-based VSLAM back-end, which is similar in spirit to the active matching solution for VSLAM front-ends [9]. *Good Graph* algorithm predicts future needs, dynamically assigns an appropriate size budget, and selects a subgraph by maximizing BA estimation conditioning. As the scene structure and motion profile change, the *Good Graph* solution will adapt the selection process and subsequent local BA optimization characteristics. The *Good Graph* algorithm is integrated into a state-of-the-art BA-based VSLAM system [24] with a cost-efficient VSLAM front-end [9]. The final VSLAM system achieves performance superior to state-of-the-art VSLAMs within multiple evaluation scenarios and computational limits (Section VI). The VSLAM system [29] and the full evaluation results [30] are released.

II. RELATED WORKS

This section first explores existing efforts on bounding the scale of the local BA problem in VSLAM. Then, algorithmic acceleration for BA solving is reviewed. Last, literature related to submodular submatrix selection, which serves as the theoretical basis behind *Good Graph*, is covered.

A. Bounding Local BA in VSLAM

VSLAM with a BA-based back-end has better accuracy and robustness than VSLAM with a filter-based back-end, as determined by the comparative study [17]. Using BA in VSLAM, especially for the high-rate local optimization module, requires bounding the scale of states to be optimized to achieve real-time or near real-time optimization rates. The

bounding leads to a local BA problem versus performing a full BA on all measurements to date.

One prevalent means to limit the problem size is to employ a sliding window strategy for the local BA [3], [18]–[22]. Only recent states (camera frames and map points) within the sliding window are optimized in local BA. Older states outside the sliding window are either dropped [3], [31] or fixed as linear priors [18]–[22]. The sliding window strategy as commonly applied in visual-inertial odometry is effective under an infinite tunnel assumption for the world structure and motion profile; it is not an optimal solution for a VSLAM trajectory with frequently revisited camera poses within the environment. The ability to reuse historical information beyond the sliding window is limited; for instance, when solely relying on loop closing. Fixing historical information to be linear priors introduces bias into the optimization, therefore leading to inferior performance under frequent revisits.

A second common strategy for bounding the scale of the optimization states is covisibility information. Covisibility approximates the amount of mutual information between keyframes [23]. Ideally, subsets of keyframes with strong mutual covisibility form well-conditioned, local BA optimization problems. For rapid queries and updates, state-of-the-art VSLAM systems [24]–[26], [31], [32] typically store covisibility information as a graph of historical keyframes, that is, as a covisibility graph. When compared with sliding-window methods, covisibility graphs encode more historical information, which is preferred in general SLAM scenarios. In the presence of revisits, a covisibility graph enables querying of earlier keyframes (and map points) for local BA; in the absence of revisits, a covisibility graph acts similarly to a sliding window. However, covisibility information offers only a rough approximation of frame-to-frame mutual information. Therefore, the actual conditioning of the optimization problems formed from covisibility graphs is not guaranteed. In practice, VSLAM systems using covisibility graphs typically over-select states in local BA, which improves the conditioning but limits the cost-efficiency of BA-based back-ends.

Yet another strategy to select optimization states involves the re-projection error [33], [34]. Before each local BA run, map points with large re-projection error are kept as optimizable states, while points with small error are treated as fixed priors. Although treating small-error points as priors does reduce the scale of local BA significantly, it may introduce bias to the size-reduced BA problem. Furthermore, the cut-off threshold of re-projection error has a strong impact on subgraph selection, and remains an open problem on its own.

B. Algorithmic Acceleration of BA Solving

Apart from bounding the scale of local BA, algorithmic accelerations to speed up BA solving have been extensively studied. Solving the least squares objective of BA problem typically involves multiple iterations, with each iteration involving a linearized system. Speeding up the linearized solution time would accelerate the BA solving. Following this observation led to a method for grouping and collapsing densely visible factors (*fragment*) into single factor, thereby reducing the

matrix-vector multiplications required in each iteration [35]. The concept of *fragment* extraction was subsequently translated to online, local BA [36]. Fragments of local BA problem are chosen online with an efficient and scalable algorithm, then used for the local BA solution. Points that are less visible are discarded from local BA. Similar to the covisibility heuristic, the visibility information is a rough approximation to the actual information. The fragments extracted don't necessarily provide guarantees on the conditioning of the size-reduced local BA problem.

Another key aspect of accelerating BA solving is exploiting the incremental structure of SLAM problem. Incremental algorithms can expedite matrix factorization, which is a computationally involved module in local BA. For example, iSAM [37] uses Givens rotations to update the QR factorization incrementally; iSAM2 [38] further eliminates the periodic batch steps for variable re-ordering and relinearization with incremental alternatives, guided by Bayes tree representations. Other work introduced incremental updates to the Cholesky factorization in BA-based back-ends [39]. Incremental algorithms for another computationally involved calculation, Schur elimination, have also been studied [40]. The combination of sliding-window and incremental algorithms improves local BA runtime [20]. The method presented in this paper has dependency upon the incremental Cholesky factorization work [39]. However, the goal of our work is complementary to these incremental BA algorithms. It pursues efficient algorithms to formulate scale-limited BA problems, while incremental approaches aim to solve a sequence of related BA problems efficiently. The cost-efficiency of the local BA problem will be further improved by combining the proposed BA formulation and incremental solving.

C. Submodular Submatrix Selection

A key aspect of this work is connecting state subset (or subgraph) selection to submodular submatrix selection. Generally, submatrix selection is NP-hard. However, shortcuts exist when the objective of submatrix selection is submodular. The submodularity of various spectral preservation objectives has been proven with regards to submatrix-selection [41], [42]. Submatrix selection with a submodular (and monotone increasing) objective can be approximated by a greedy method with an approximation guarantee.

Prior work exists regarding speeding up SLAM modules by selecting a subset of states based on a submodular objective function. Initially, submodularity and selection led to accuracy improving and nearly cost-neutral implementations [43], [44], or to accuracy improving but more costly implementations [45] (but still faster than combinatorial selection). The important idea advanced was the value of submodular objectives to facilitate data-association between keypoints detected in the front-end and map points from the back-end. The idea then led to the design of a cost-saving active feature matching algorithm based on maximizing a submodular objective with accuracy neutral outcomes [9]. The active matching front-end was demonstrated to reduce computational load while preserving pose estimation performance. Submodularity to

reduce the cost or size of the general BA problem has also been explored. The 2D pose graph solution and its optimality was related to graph connectivity, which was quantified by the weighted number of spanning trees (WST) within the graph [46]. By proving that WST is monotone log-submodular, a greedy solution was presented to find a subgraph that approximately optimizes the WST. Our work is similar to [46] for subgraph selection in BA problems using submodular objective functions. However, the type of BA problem targeted in our work is the time-sensitive local BA of 3D SLAM, while the problem considered in [46] is primarily the global optimization of a 2D pose graph. Accordingly, the subgraph selection algorithm proposed in this paper deals with a more densely connected graph structure, and has a stricter compute budget for selection. To that end, we work directly with the conditioning of the optimization problem rather than with the graph analog, which provides improved cost-efficiency of the local BA problem in a state-of-the-art VSLAM system when applied to practical and challenging scenarios.

To further speed up the greedy selection process under submodular objective functions, randomized acceleration may be incorporated into the greedy submatrix selection iterations. The greedy method with randomized acceleration, which we call *lazier greedy*, has near-optimal performance guarantees [27]. There are incremental and distributed implementations of the lazier greedy method [28]. Introducing the lazier greedy algorithm into the VSLAM front-end through an approach called *Good Features* matching, provided sufficient time savings to run the selection process in real-time [9]. Compared to the local BA problem of the back-end, the data-association submatrix selection problem of *Good Features* matching is relatively small. The matrix processed in this work is the system matrix of a local BA problem, which easily reaches thousands of rows and columns. The proposed *Good Graph* algorithm extends the lazier greedy idea with key improvements tailored to the local BA of VSLAM back-ends.

III. PRELIMINARY

Consider the least squares objective of a general BA problem:

$$\arg \min_{\mathbf{x}_c, \mathbf{x}_p} \sum_{i,j} \|\rho(\mathbf{x}_c(i), \mathbf{x}_p(j))\|_{\Sigma_{ij}}^2, \quad (1)$$

where \mathbf{x}_c is the vector of camera states, \mathbf{x}_p is the vector of map states, ρ is the residual function (e.g. the on-frame distance between measurements and world-to-frame projections). The covariance of each residual term, Σ_{ij} , is included when available.

Numerical solutions to the non-linear objective (1) commonly employ iterative methods based on the Gauss-Newton or Levenberg-Marquardt algorithms. Each iteration computes a linear approximation of the original objective within the trust-region around the current estimate:

$$\arg \min_{\delta} \|\mathbf{J}\delta - \mathbf{b}\|^2. \quad (2)$$

Solving the linear system (2) is equivalent to solving the normal equation

$$\mathbf{\Lambda}\delta = \boldsymbol{\eta}, \quad (3)$$

where $\Lambda = \mathbf{J}^T \mathbf{J}$ and $\boldsymbol{\eta} = \mathbf{J}^T \mathbf{b}$. The spectral property of the system matrix Λ is important for two reasons: 1) a well-conditioned Λ suggests fast convergence for iterative solvers and 2) the volume of Λ is connected to the information or uncertainty level of the corresponding BA problem.

For ease of specification and interpretation, the BA problem is sometimes represented as a factor graph [47]. To support interpretation of the *Good Graph* approach, a factor graph interpretation will be used, with the following terminology: *vertices* represent state entities (e.g. a camera or map point), *edges* represent measurements, and the term *graph*, representing the BA problem, consists of the *vertex* and *edge* sets.

Due to the (worst case) cubic complexity of BA solving, working on a subproblem of the original BA with a smaller scale could be more cost-effective if the full BA solution is not required. We are therefore interested in selecting a subgraph of the full graph (i.e. of the full BA problem). As discussed earlier, the spectral properties of the system matrix are important for BA solving. It is desirable to select a subgraph with less states while preserving the spectral properties of the corresponding system matrix.

One important spectral property of a system matrix is quantified by *logDet*, which has been applied to guide the feature selection [45] and active matching [9] of VSLAM. Compared to other metrics such as the *condition* and *minimum eigenvalue*, *logDet* aligns with the goal of cost-efficiency. It is strictly submodular, which enables efficient selection algorithms. Computing *logDet* involves Cholesky factorization, which is cheaper than other commonly involved factorizations such as QR and SVD. Finally, *logDet* captures the necessary spectral properties of matrix conditioning for solving linear systems of equations.

Using the *logDet* metric, the *Good Graph selection* objective is formulated as a submatrix selection problem:

$$\max_{\mathbf{S} \subseteq \{0, 1, \dots, m+n-1\}, |\mathbf{S}|=k} \log \det([\Lambda(\mathbf{S})]), \quad (4)$$

where the complete system matrix Λ contains m camera states and n map states, \mathbf{S} is the index subset of the selected camera and map states, $[\Lambda(\mathbf{S})]$ is the corresponding submatrix, and k is the cardinality constraint. The choice of states (vertices) is optimized with the submatrix selection objective (4), while the choice of non-zero fillings (edges) is conducted implicitly. The selection process finds a subgraph with fewer vertices than the full graph, but which retains the connectivity of the chosen vertices; the sparse structure of the subgraph is preserved.

IV. GOOD GRAPH SELECTION IN GENERAL BA

The optimal submatrix selection objective (4) finds an optimal subgraph (i.e., *Good Graph*). Ideally, the result will lead to a well-conditioned submatrix, as illustrated in the second column of Fig. 1. The corresponding subgraph, visualized in the first column of Fig. 1, meets the cardinality constraint and maximizes *logDet*. However, the problem described by (4) is an NP-hard combinatorial optimization problem, whose solution will usually be more expensive to solve than the original least-squares BA. Instead of tackling the original problem (4), two relaxations are proposed to reduce the

computational cost while providing sub-optimality guarantees, plus the incremental structure of the problem is exploited to avoid repeated computation.

A. Subgraph Selection on Camera-only System

In practice, there are issues working with the complete system matrix Λ . The large size of Λ negatively impacts submatrix selection efficiency. Additionally, submatrix selection from the joint set of camera and map point states may create undesirable behavior due to the relationship between map points and camera views [45]. A common practice in bundle adjustment is to marginalize out the map states with Schur elimination. The marginalized matrix will involve only camera states:

$$\mathbf{M} = \Lambda_{cc} - \Lambda_{cp} \Lambda_{pp}^{-1} \Lambda_{cp}^T, \quad \Lambda = \begin{bmatrix} \Lambda_{cc} & \Lambda_{cp} \\ \Lambda_{cp}^T & \Lambda_{pp} \end{bmatrix}. \quad (5)$$

The top of the fourth column of Fig. 1 shows an example of a marginalized matrix \mathbf{M} with the corresponding camera-only graph at the top of the third column. The size of \mathbf{M} is smaller than that of Λ . The original submatrix selection objective (4) is replaced by the submatrix selection objective of the marginalized, camera-only matrix \mathbf{M} :

$$\max_{\mathbf{S} \subseteq \{0, 1, \dots, m-1\}, |\mathbf{S}|=k} \log \det([\mathbf{M}(\mathbf{S})]), \quad (6)$$

where k constrains the camera states only. Objective (6) for a camera-only system is not equivalent to the original objective (4). Ideally, a subgraph selected with (4) would have better conditioning, since both camera and map states could be selected explicitly. However, optimizing (4) is expensive, operates over different states with different properties, and may lead to inconsistency during the optimization. Map states are selected implicitly in the more efficient and consistent camera-only objective (6). All map points visible to the selected camera subset are taken. The camera state selection process is visualized in the second row of Fig. 1(b). The third row shows the recovered camera and map subgraph obtained by including all map points visible to the selected cameras.

At this juncture, there is a choice to make regarding the map points visible to only a single camera from the subset: keep them or remove them. When kept, the map points measured by only a single selected camera view serve as priors. Their effect will depend on the structure of the BA problem created by the selected subgraph. General large-scale BA solves an over-determined system, where the loss of the priors will not significantly impact *logDet* maximization. These priors may introduce bias as any measurement error associated to the measurements cannot be corrected. To avoid introducing bias to the subgraph (and downstream BA), these map points are ignored and not used to build the BA subgraph. As will be shown later in Fig. 3(c), the *logDet* value drop for the final subgraph obtained by discarding single-view priors is relatively small. On the other hand BA-based VSLAM back-ends solve a smaller sized BA problem. Removing all map point priors will have a relatively larger impact on the solution. Furthermore, the bias introduced by map point priors will not be as detrimental since the BA-based back-end improves

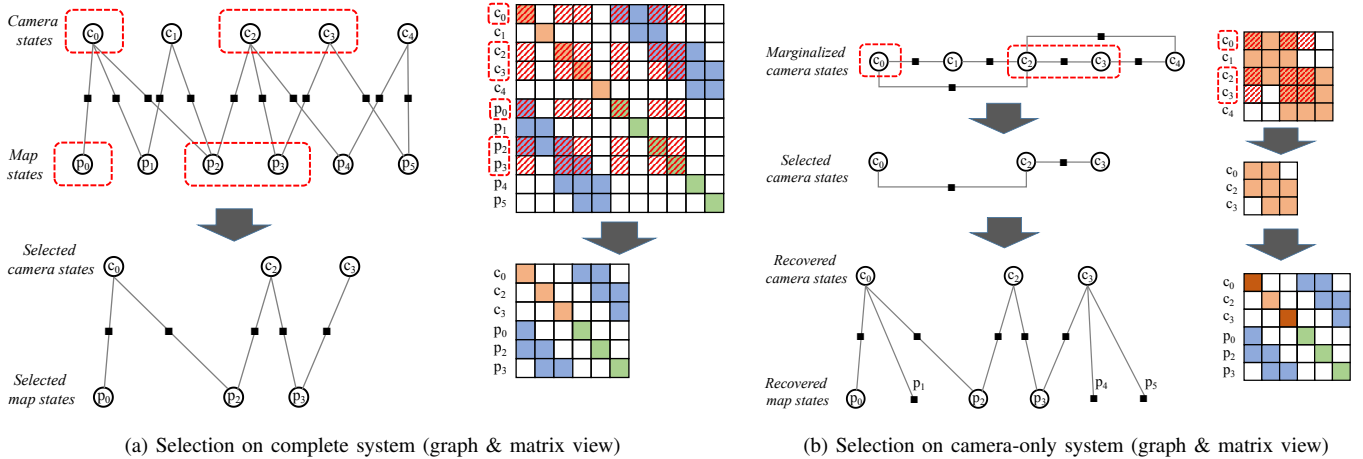


Fig. 1. Toy example of subgraph selection on a complete system vs. camera-only system. Working with a camera-only system is desirable for improved efficiency. Compared with the ideal subgraph selected from the complete system, the subgraph selected from the camera-only system (and recovered to include map states) will include priors of the points measured once by the selected cameras, e.g., points p_1 , p_4 and p_5 . In general BA, we simply discard all priors from the selected subgraph. In BA-based VSLAM, we keep the priors of points optimized at least once in previous BA runs.

map state estimation periodically. Keeping track of whether a map point has been optimized or not by local BA iterations permits selective use of map points as priors. In VSLAM back-end implementations of *Good Graph*, priors from map points that have been optimized at least once before will remain in the final subgraph. Map point priors that have not yet been processed by a local BA cycle are ignored.

B. Submatrix Selection with Lazier Greedy

Though the camera-only objective (6) involves combinatorial selection from a smaller set, it is still NP-hard. To efficiently solve the camera-only objective while limiting the loss in optimality, the submodularity of the *logDet* set function is exploited. The *logDet* function is submodular and monotone increasing [41]. Submodularity is extremely useful. It indicates that the combinatorial optimization objective (6) can be approximately solved with greedy methods.

Theorem 1: [48] Given a normalized, monotone, submodular set function $f : 2^F \rightarrow \mathbb{R}$, whose optimal solution to the maximization problem (6) is denoted by S^* , then the set $S^\#$, computed by the greedy heuristic, is such that:

$$f(S^\#) \geq (1 - 1/e)f(S^*) \approx 0.63f(S^*).$$

The bound in Theorem 1 ensures that the worst-case performance of a greedy algorithm cannot be far from optimal. The $(1 - 1/e)$ approximation ratio is the best ratio any polynomial algorithm can achieve (assuming $P \neq NP$) [49].

The camera-only objective (6) can be solved with a greedy method as follows. Starting from the submatrix $M(0)$ of an initial camera vertex (i.e., the most recent keyframe), the algorithm iteratively searches for the best submatrix that has one more state than $M(0)$. After $k-1$ iterations, the submatrix contains k camera states and selection stops. Finally, all map states that are visible by the chosen cameras are included. The computational complexity of greedy method is $\mathcal{O}(km)$.

Inspired by earlier active matching work [9], a lazier greedy algorithm [27] is utilized to further improve the solve time of (6). In contrast with the greedy method, the lazier greedy

method only evaluates a random subset of candidate states (row and column blocks) at each iteration. The size s of the random candidate subset is controlled by a decay factor ϵ : $s = \frac{m}{k} \log(\frac{1}{\epsilon})$. The computational complexity of the lazier greedy method is $\mathcal{O}(\log(\frac{1}{\epsilon})m)$, which is lower than the $\mathcal{O}(km)$ complexity of the greedy method. Furthermore, the approximation ratio of the lazier greedy method has an ϵ -controllable drop from that of the greedy method:

Theorem 2: [27] Let f be a non-negative monotone submodular function and set $s = \frac{m}{k} \log(\frac{1}{\epsilon})$. Then lazier greedy achieves a $(1 - 1/e - \epsilon)$ approximation guarantee in expectation to the optimum solution of (6).

Theorem 3: [50] The expected approximation guarantee of $(1 - 1/e - \epsilon)$ is reached with a minimum probability of $1 - e(-0.5k(\sqrt{\mu} + \ln(\epsilon + e^{-1})/\sqrt{\mu})^2)$, when maximizing a monotone submodular function under the cardinality constraint k with lazier greedy. $\mu \in (0, 1]$ is the average approximation ratio when maximizing the margin gain during each iteration of lazier greedy.

The ϵ drop balances the speed of execution versus the approximation guarantee. How to mediate these two will depend on the problem being solved and the typical sizes of k and m . For all experiments performed in later sections, the decay factor ϵ is set to 0.0025 (i.e., $1/400$). With this value, lazier greedy selection has a logarithmic drop in computational cost, while preserving the approximation guarantee of the optimal solution (a small linear drop in expectation, with a minimum probability close to 1). The expected runtime is $\mathcal{O}(6.0m)$ versus $\mathcal{O}(km)$ for the greedy method, with typical values of k ranging within 20 – 60 during local BA optimization by VSLAM back-ends.

C. LogDet with Incremental Cholesky

One bottleneck of the lazier greedy algorithm is the cost of computing the *logDet* metric. For the positive definite square matrix M , efficient computation of *logDet* involves Cholesky factorization. For $M = LL^T$, $\log \det(M) = 2 \sum \log(\text{diag}(L))$. However, simply using a Cholesky-based

$\log\text{Det}$ computation within the lazier greedy algorithm will not provide a speed improvement. The size of the selected submatrix grows linearly as a function of the lazier greedy iterations, while the Cholesky factorization cost grows cubically, which affects the cost-efficiency of submatrix selection.

Given that the submatrix is incrementally built during the selection process, the Cholesky factorization in the $\log\text{Det}$ computation should likewise be obtained incrementally. Doing so reduces the cost to evaluate $\log\text{Det}$. Therefore, with each iteration of the lazier greedy algorithm, the system matrix of the current selection, dubbed $\mathbf{M}(i)$, will be partially updated. The partial updates involve appending the updated blocks to the rows and columns of the existing matrix $\mathbf{M}(i)$:

$$\mathbf{M}(i+1) = \begin{bmatrix} \mathbf{M}(i) & \mathbf{B} \\ \mathbf{B}^T & \mathbf{D} \end{bmatrix}. \quad (7)$$

Given the Cholesky factorization $\mathbf{L}(i)$ of $\mathbf{M}(i)$, the Cholesky factorization of new submatrix $\mathbf{M}(i+1)$ is [51]:

$$\begin{aligned} \mathbf{L}(i+1) &= \begin{bmatrix} \mathbf{L}(i) & \mathbf{L}_1 \\ \mathbf{0} & \mathbf{L}_2 \end{bmatrix}, \\ \mathbf{L}_1 &= (\mathbf{L}(i)^+)^T \mathbf{B}, \\ \mathbf{L}_2 &= \text{chol}(\mathbf{D} - \mathbf{L}_1^T \mathbf{L}_1). \end{aligned} \quad (8)$$

Computing $\log\text{Det}$ with the incremental formula (8) further improves the cost-efficiency of Good Graph selection.

D. Implementation Details and Validation

Besides the three algorithmic improvements just described, the base Good Graph algorithm includes one additional improvement, while the SLAM-focused Good Graph algorithm further adds one more, with both based on good engineering practice. The former involves using an analytical form of the Jacobian for generating the system matrix $\mathbf{\Lambda}$ [52]. Having a closed-form function for the Jacobian is more efficient than using numerical schemes. The latter exploits the fact that typical VSLAM back-ends already limit the local BA problem size based on covisibility constraints. Thus, there is a flag to bound the candidate pool of camera states based on the covisibility graph as the source candidate set, which is faster to run subselection for than using all camera vertices as the source set (due to the $\mathcal{O}(\log(\frac{1}{\epsilon})m)$ cost). The covisibility bounded *Good Graph* sets the flag to true. All of these elements comprising the *Good Graph* algorithm were integrated into a state-of-the-art BA solver, SLAM++ [53]. For less-constrained applications such as general BA, a mixed approach can be pursued, where the covisibility candidate pool extends to more camera vertices with second-order or higher neighbors of the covisibility graph.

To validate the cost-efficiency of the *Good Graph* algorithm, three experiments were conducted: two with a general BA dataset, the Venice dataset [54], which includes 871 cameras and 530k map points; the other on randomly generated BA problems with 50 cameras and 6k map points, which simulates the problem of local BA in VSLAM back-end. In all three experiments, the BA solver SLAM++ is configured with a maximum iteration number of 20.

TABLE I
PROPOSED IMPROVEMENTS COVERED BY GOOD GRAPH VARIANTS

Variants	A	B	C	D	E
Camera-only	✓	✓	✓	✓	✓
Lazier Greedy	✗	✓	✓	✓	✓
Incremental Chol.	✗	✗	✓	✓	✓
Analytical Jacob.	✗	✗	✗	✓	✓
Covis-bounded Pool	✗	✗	✗	✗	✓

1) *General BA Subgraph Selection Ablation Study*: The study with the 871-camera Venice dataset is an ablation type of study on the *Good Graph* algorithm. Five *Good Graph* variants, consisting of incrementally applied modifications to arrive at the full VSLAM *Good Graph* variant are applied to reconstruct the Venice scene. The full BA with all camera and map states is also evaluated to serve as a reference. Table I describes the incremental implementation schedule and variant letter assignment. Each variant selects an 87-camera subgraph from the full graph, for input to the SLAM++ BA solver. All computations are executed on a PC (Intel i7-7700K, PassMark 2583 per core). Problem size, timing, and error statistics for all implementations are reported in Tables II - IV.

Time cost breakdowns of the full BA and the five GG variants are reported in Table II. Initially the time cost increases, which is the common issue for active approaches that aim to reduce problem size. Optimization-based active selection can take longer to run than the time saved. However, as additional algorithmic shortcuts are incorporated, the problem reduction time cost improves. The time consumption of *Good Graph* variant *E*, which covers all improvements described, is the lowest of all six methods. Each improvement described above had a clear, positive impact on the cost-efficiency of *Good Graph* selection. To understand whether the implementations lead to improved performance, Table III looks at the time cost per map point optimized. It factors out the effect of the problem size on the solution time cost. It is not until the last variant (*E*) that the time cost to solve per point becomes lower than the full BA time cost per point.

The map point accuracy of the BA solutions is also evaluated with the RMSE between the 3D points optimized by the tested implementations and the ground truth points. The fixed number of iterations in the optimization loop provides a means to evaluate the convergence efficiency of the methods. However, each implementation will optimize different sets of 3D points, which might serve to confound the RMSE statistics. Therefore, Table IV contains the RMSE of all map points optimized per variant, and on the subset of points common to all methods, which is the intersection of 3D map points selected by all five variants. Though selecting the same number of cameras (i.e., 87) as other variants, variant *E* appears to have a higher percentage of high-quality points that improve the optimization conditioning based on having the lowest RMSE error. Selection from the covis-bounded pool ensures strong covisibility between selected cameras. Moreover, it is less likely to take points with single-views, which are considered to provide a biased prior and are discarded before BA solving.

TABLE II
TIME COST BREAKDOWN (MS) OF GOOD GRAPH VARIANTS

Variants		Full	A	B	C	D	E
Subgraph	Jacob.	-	6,531	6,902	6,628	5,787	456
	Schur	-	3,409	3,499	3,426	3,408	221
	Chol.	-	80,153	3,990	148	131	46
	Misc.	-	28,695	110	272	264	80
	Total	-	118,788	14,501	10,474	9,590	803
BA Solving		46k	31,791	17,953	17,685	5,740	2,839
Total Time		46k	150.1k	32.5k	28.2k	15.3k	3.6k

TABLE III
TIME COST (SELECTION & BA) PER POINT PROCESSED ($\mu\text{s}/\#$)

Variants	Full	A	B	C	D	E
Time	86.7	1,217.7	266.0	230.1	124.6	52.8

TABLE IV
GRAPH SCALE AND RMSE (MM) OF BUNDLE ADJUSTMENT

Variants		Full	A	B	C	D	E
Scale	Cam.	871	87	87	87	87	87
	Point	530k	124k	122k	122k	123k	69k
RMSE	All	49.2	41.9	45.7	45.7	41.2	39.7
	Int.	49.3	41.8	45.7	45.7	41.1	39.8

Overall, the full *Good Graph* exhibits the best time cost per point processed and the best RMSE error, which indicates that the full *Good Graph* selection process is efficient and achieves the desired goal of improving the conditioning of the optimization problem. Though less points are processed when compared to the *Full* problem, this factor is not problematic. Having well conditioned points to match against during the local map pose optimization process in the front-end is the main objective of *Good Graph*. If *Good Graph* were to be sought for the full BA optimization, then additional steps would be required to incrementally incorporate new camera views and map points in a manner that does not compromise the existing optimized states. Running additional iterations of *Good Graph* with properly weighted costs might provide an improved solution over the full optimization, without compromising run-time.

2) *General BA and Subgraph Selection*: Secondly, the full-featured *Good Graph* algorithm (i.e., variant *E*) is compared against two subgraph selection heuristics: 1) covisibility-based selection (also called max-covis here), and 2) random selection. Covisibility-based selection first ranks the cameras based on the number of covisible points shared with the initial camera vertex, then takes the top- $(k - 1)$ cameras and corresponding covisible points to construct a small BA problem. Random selection takes camera vertexes randomly from the full set, as well as the corresponding covisible points observed by the selected camera subset. Both are simpler, more light-weight selection heuristics than *Good Graph* (without covisibility bounding). The outcomes are illustrated in Fig. 2, with the RMSE computed for all points selected by the methods (all), and for the points all methods have in common (int). Compared with the two heuristics, *Good Graph* selects more

points while achieving lower RMSE after subgraph BA. As a mixture of spectral property maximization and covisibility bounding, *Good Graph* selection finds a better subgraph, quantitatively and qualitatively, than the purely covisibility-driven selection. Random sampling, on the other hand, can be seen as an extreme case of *Good Graph* selection: in each iteration of lazier greedy, only 1 sample is randomly taken for evaluation. According to Theorem 2, random sampling is equivalent to lazier greedy selection with $\epsilon = e^{-\frac{k}{m}}$. The approximation ratio of random sampling is $1 - 1/e - e^{-\frac{k}{m}}$ in expectation. Due to the looser guarantee on performance, random sampling may end up with the worst performance of the three subgraph BA methods tested: it may take more time to process per point, and may have the highest RMSE. Here that does happen.

The plotted point clouds based on the selected cameras in Fig. 2 shows that the *Good Graph* selection picks different points when compared to the covisibility method. The lower RMSE values for (all) and (int) of the *Good Graph* solution indicates that the selected camera and point combinations have better conditioning, since the number of optimization iterations is constant across the implementations. The max-logDet objective function can provide better camera selections than the max-covis and random selection heuristics. Meanwhile the time cost per point of *Good Graph* lies near the average of the values obtained for the *Full* and *Covisibility* implementations (which is $57.2 \mu\text{s}/\text{pt}$). There is the added cost of identifying the *Good Graph* in order to improve the conditioning of the BA problem. These two competing factors lead to an error vs compute trade-off in identifying a smaller BA problem. Balancing this within a SLAM system will require additional modifications to the baseline *Good Graph* implementation.

3) *Local BA with Sequential Camera Poses*: The last experiment further validates the reconstruction accuracy and BA conditioning of the *Good Graph* algorithm with a randomized simulation of a small-scale BA problem, designed to resemble the local BA of VSLAM back-ends. The simulation scenario includes a 6DoF trajectory consisting of 50 cameras and a total of 6000 map points. The cameras move in a uniform circular motion, while the map points are randomly instantiated in the scenario. To guarantee the conditioning of the constructed BA problem, the following conditions are enforced: each point is visible from at least 2 cameras, and each camera observes at least 20 points. Subgraphs are selected with 9 desired cardinalities: from 10% to 90% of cameras from the 50 cameras. Under each desired cardinality, a subgraph is selected using the proposed *Good Graph* algorithm (*GG*) without covisibility bounding, and solved as a small BA problem. Two heuristics, as introduced in the previous experiment, are included as well: covisibility-based selection (*Covis*), and random selection (*Rand*).

The simulation results of 100 random configurations are summarized in Fig. 3. At the extremes (e.g., very few points or almost all points), the methods have similar performance, c.f., Fig. 3(a). The *logDet* versus graph scale plot qualitatively shows less separation of conditioning between the three methods, while there is a more easily seen gap between *Good Graph* conditioning and that of the other methods for subgraph

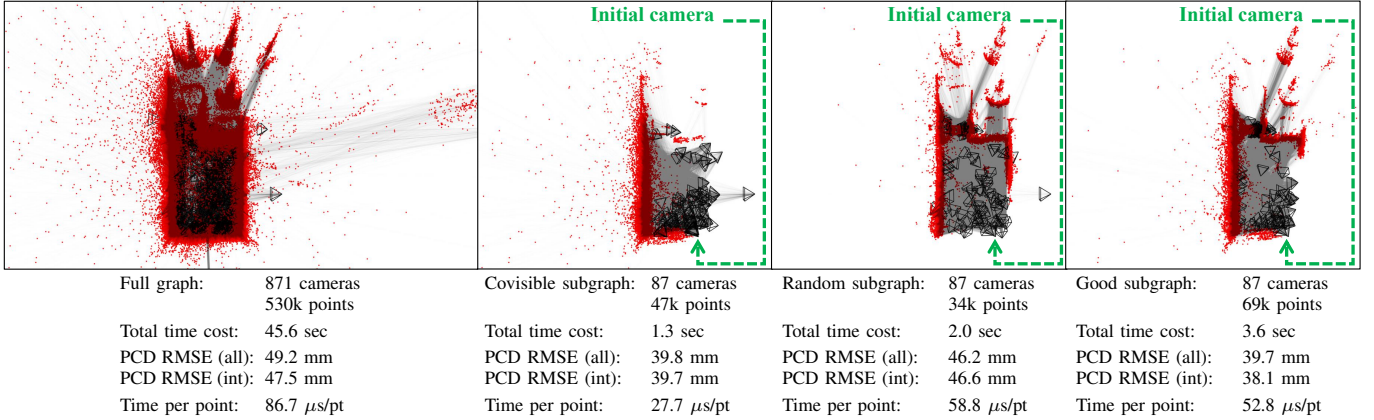


Fig. 2. BA example on Venice dataset [54]. **From left to right:** 1) BA on full graph; 2) BA on subgraph selected with covisibility information; 3) BA on subgraph selected randomly; 4) BA on subgraph selected with proposed Good Graph algorithm. All three subgraphs start with the same camera (i.e., initial vertex). The time cost of subgraph BA is less than that of full graph BA. Compared with covisible and random subgraphs, BA on the good subgraph has better 3D reconstruction accuracy (lower RMSE in the reconstructed point cloud), while processing twice amount of 3D points.

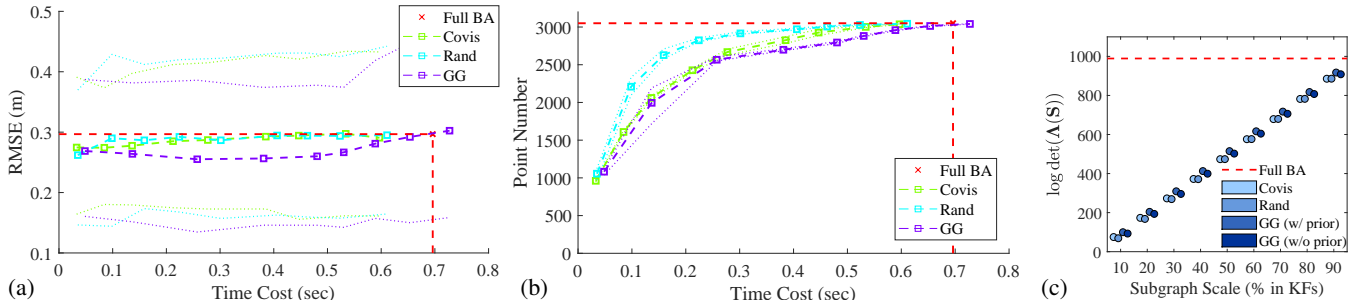


Fig. 3. Cost-efficiency of full and subgraph BA in simulated scenarios. **Left:** total time cost (of subgraph selection and BA) vs. reconstruction error (RMSE of 3D point cloud) for full BA and three subgraph BA. The average point of full graph BA under 100-repeat is marked with red cross. Meanwhile the average curve of subgraph BA under different subgraph scales is in square and dashed line. The first and third quarter curves of subgraph BA in 100-repeat are also plotted with dotted lines. **Middle:** total time cost vs. number of map point optimized in BA, using the same plotting style as previous. **Right:** boxplot of submatrix $\log \det$ scores in subgraph BA, under different subgraph scales. The average $\log \det$ of full system matrix is in red dashed line.

scales between 30-70%, which manifests as lower RMSE for those scale values. For most cases local BA with *GG* has better accuracy than the other two heuristics, given the same amount of time for subgraph selection and BA solving. In essence, there exist *GG* configurations that can outperform random and covisibility selection for non-extremal selection percentages. When the desired subgraph cardinality reaches 80% or higher, the RMSE of *GG* BA increases to the same level of the other subgraph BA methods and the full BA. In such cases there is little value in using *GG*. While this observation suggests some limits to *GG* improvements for high subgraph cardinality, it is less of a concern in practice; most *GG* calls in SLAM will be triggered with subgraph cardinalities below 80%.

The analysis provides further indication that the camera states chosen by *GG* generate a fundamentally different set of map points than those from *Covis*, with chosen camera states that may have poor covisibility but strong baseline matches. The *GG* approach is also not trying to maximize map points since random selection leads to larger BA configurations (except at 10%), per Fig. 3(b). Additional support for the assertion lies in the $\log \det$ scores for the selected submatrices using different subgraph selection methods, c.f. Fig. 3(c). Under each desired subgraph cardinality, the submatrix selected with *GG* has higher $\log \det$, which indicates the effectiveness of the

GG algorithm at finding camera poses with good overall BA conditioning. The improvement holds regardless of whether the priors for map points with single camera measurements are included or ignored, with inclusion giving better conditioning.

V. BUDGET-AWARENESS OF LOCAL BA IN VSLAM

The *Good Graph* algorithm boosts the effectiveness of solving both general and local BA problems given a root camera vertex and fixed number of iterations in the numerical optimizer. When combined with several sensible modifications to improve run-time performance, the time cost to establish a better conditioned BA sub-problem from the root camera is a fraction of the final BA solution time cost. As with the earlier *Good Feature* work [9], *Good Graph* for SLAM will be an active optimization approach that is time-cost aware with the goal of optimizing the computational budget to improve output performance metrics (here, map RMSE and subsequently pose RMSE). In this context, active optimization means an approach that actively selects from available data to define an optimization problem whose limited scale solution provides low-error estimates, and with more predictable and consistent optimization times. What remains is to establish a mechanism for adaptively implementing the *Good Graph* algorithm within an on-board SLAM system.

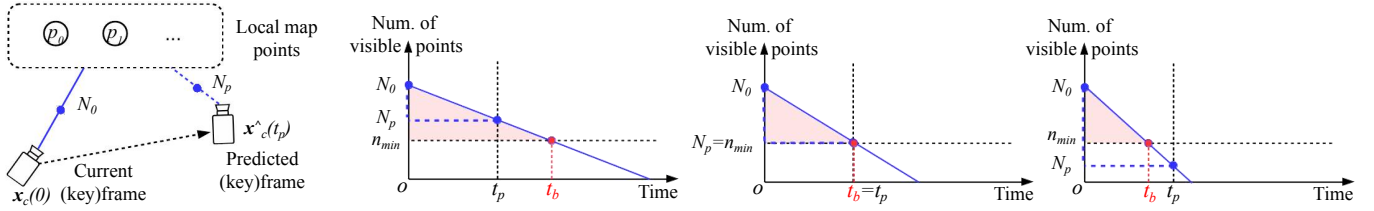


Fig. 4. Linear prediction of local BA budget, where the camera pose in the near-future, $\widehat{\mathbf{x}}_c(t_p)$, is assumed available from controller or IMU propagation. The number of remaining-visible local map points N_p is decisive in BA budget prediction. Given the relative order between N_p and a pre-set minimal number n_{min} , three typical cases are illustrated: loose-budget, well-balance and tight-budget.

Compared to more general use of BA, one key aspect of local BA within VSLAM back-ends is the impact of optimization time on performance. The local BA should be solved in time to contribute to the local pose estimation front-end process: longer-than-expected BA processing could cause drift or even track failure, especially for platforms under fast movement. Thus, online implementation requires a mechanism to bound the problem size to meet anticipated time budget constraints. Optimization time and BA problem size are directly related quantities. Thus, the objective of this section is to communicate a strategy for determining the time budget of the local BA problem, as well as the size k of the desired *good subgraph*. The desired size k versus the current size of the (covisibility-limited) local BA problem will determine whether to trigger the *Good Graph* selection process or not.

A. Predicting Budget of Local BA

The primary role of the local BA in VSLAM is to provide accurate map points as localization references for future camera frames. When few map points will be visible in future camera frames, it is necessary to execute local BA at a fast rate so that estimates of new map points converge in time. When sufficient map points will be present in future frames, the local BA can run at a slower rate to provide a complete and fully-optimized map. In effect, the budget of the local BA problem should be related to the number of visible map points in future frames.

Similar to the feature selection work [45], camera poses (with noise) are assumed to be available in the near future. This assumption is reasonable: for closed-loop systems such as robots, future poses are available from the trajectory tracking controller or the trajectory planner. For open-loop systems such as AR headsets, near-future poses can be predicted by propagating IMU measurements. Given future camera poses up to t_p seconds from the current time, there will be a set of visible map points that project to the predicted camera views, whose cardinality is N_p . Now, assume that this quantity of visible map points decays linearly with time, defining a function $N : \mathcal{R}^+ \rightarrow \mathcal{N}$ where the argument is time into the future. The local BA time budget should be such that the map point estimates are improved prior to losing visibility for a significant fraction of them.

The value $N(0) = N_0$ is the number of points visible in the current (key)frame. The predicted triplet of values (N_0 , N_p , and t_p) form a triangle in the number of visible features versus time advance graph, see Fig. 4 (blue dash-dotted triangle). It

defines the slope of the assumed linear loss function $N(\cdot)$. Given an acceptable lower limit of remaining points n_{min} and the current amount of visible points $N(0)$, there will be a time point t_b at which $N(t_b)$ decays to the minimum acceptable quantity of visible map points n_{min} based on the assumed linear loss in visibility. These variables ($N(0)$, n_{min} , and t_b) define a different triangle (shaded triangles), and can have a different size relative to the predicted triplet triangle. The ratio of the triangle areas is an indicator of time excess or insufficiency. It can be used to modulate up or down the local BA time budget t_b based on similar triangles geometry for the case that there is reduced map point visibility into the future:

$$t_b = \begin{cases} \frac{N_0 - n_{min}}{N_0 - N_p} t_p & \text{if } N_p < N_0 \\ t_{max} & \text{otherwise} \end{cases} \quad (9)$$

If there are more map points visible in the future than at the current time, then the local BA problem is presumed to be well-conditioned as there are many points available. The back-end has most likely optimized the points already such that they will sufficiently inform pose estimation along the planned or predicted camera trajectory. There is no need to limit the local BA budget in order to generate well conditioned map points sooner, thus the local BA process is given a larger time allocation t_{max} . The main parameters were set as follows: $t_p = 500$ ms, $t_{max} = 800$ ms, and $n_{min} = 240$ points.

The time allocation provided will be scenario dependent as the triangle generated will fluctuate with N_0 and N_p , which depend on what has been measured and what will be measured. It is data-adaptive. The local BA budget predicted with (9) implicitly reflects structure and motion information. Three typical cases of local BA budget outcomes based on the linear visibility loss model are illustrated in Fig. 4, which are determined by the predicted visible points N_p being larger than, equal to, or less than the preset minimum points n_{min} , as seen from left to right. The first case maps to a larger budget since the predicted loss is not as bad as the largest acceptable loss (which hits the lower limit). The area of the triangle is smaller, meaning that there is extra time to perform back-end calculations. It is likely to occur when the scene structure is texture-rich, as abundant map points are visible, or when the camera motion is slow, as most points remain visible because of the small parallax. The third case maps to a smaller budget since the predicted loss goes below the acceptable limit. The opposite relationship occurs, in that the predicted triangle has more area than the largest acceptable triangle

under the comparable linear loss rate. It suggests reducing the time allocation in order to more rapidly estimate the few map points that are anticipated to be visible in the near future. This latter case typically appears when the future world structure has limited texture or the camera is moving rapidly. In the equality case, the expected amount of visible map points, the estimation convergence rate of trajectory visible map points, and the optimization time cost of the back-end process are presumed to be in balance.

B. Determining the Size of Good Graph

Given a certain budget t_b for the local BA problem, a comparably sized subgraph needs to be selected for use within the *Good Graph* algorithm so that the downstream local BA solution time fits within the target time budget. The key parameter to be sent into the *Good Graph* selection is the desired subgraph size k , characterized by the number of keyframes. The relationship between t_b and k will vary based on the available computation. It must be empirically derived, either beforehand or during online operation.

In either case, the easiest manner to establish the necessary relationship between t_b and k is to regress on the function predicting the time from the keyframe quantity, $t_b = \hat{t}(k)$, based on empirically measured local BA times to problems of different sizes computed on the target device. Inversion of the function gives the desired mapping $k = \hat{k}(t_b) = \hat{t}^{-1}(t_b)$. Fig. 5 provides two example functions used in the experiments and the source data leading to the regressed curves. One regressed function is for a PC with an Intel CPU, and the other is for an embedded device with an ARM SoC. The dependence should be at worst cubic, therefore a cubic polynomial fit is regressed. During run-time, the *Good Graph* local BA size will be determined by the inverse mapping $k = \hat{k}(t_b)$ and the time budget to meet. Plotted along with the curves is the nominal time budget (t_p) to use during predicted feature loss and the maximal time budget (t_{max}) to use during predicted feature increases. These map to hardware-dependent keyframe limits.

C. Integration to Local BA in VSLAM

Given a mechanism to establish the desired size k of the good subgraph, the final step is to specify the nature of the *Good Graph* selection process in a manner compatible with the VSLAM system. Earlier, Section IV-D explored the implementation of *Good Graph* from two perspectives: the construction of the maximally sized problem (up to k) given all possible camera graph vertices, and the construction of a covisibility informed subset. It concluded that the most sensible augmentation for VSLAM would be to sub-select from the covisible set since existing VSLAM methods will typically already form the local BA problem based on covisibility [55]. However, that leads to another interesting data-adaptive outcome that establishes whether to trigger *Good Graph* or not: the desired graph size versus the covisibility graph size. If the desired subgraph size k is equal or larger than the size m of the candidate pool based on covisibility, *Good Graph* sub-selection is skipped and the entire covisibility subgraph establishes the local BA optimization. If instead

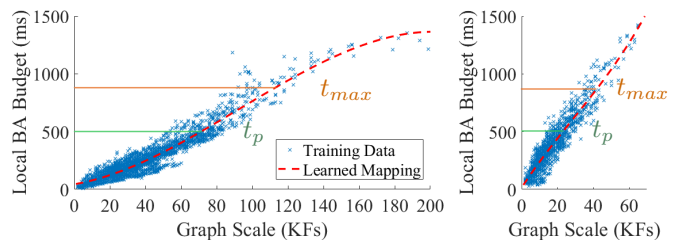


Fig. 5. Mappings between keyframe number and local BA budget, on two target devices. **Left:** mapping learned on PC with Intel i7-7700K CPU. **Right:** mapping learned on Jetson TX2 with ARM SoC (Cortex A57).

$k < m$, then *Good Graph* selection is triggered and $k - 1$ historical keyframes will be sub-selected from the candidates. The output good subgraph with k keyframes (including the current one) will (approximately) maximize the conditioning of the local BA problem seeded with the current estimate, i.e., with the most recent keyframe.

One additional modification is made to improve the overall local BA optimization with regards to the planned or predicted future state of the camera. Instead of only taking the most recent keyframe as the initial selection in *Good Graph*, we can further weight the selection to those keyframes (and, implicitly, the map points) that are informative to future estimates. Predicting the budget of local BA requires predicting the camera pose and the visibility of map points in the near-future. The predicted camera pose should be exploited to create a local BA problem attuned and conditioned to where the camera will be t_p seconds into the future. One means to do so is to create a virtual keyframe with the predicted map measurements at this predicted camera pose $\hat{x}_c(t_p)$. The *Good Graph* selection algorithm for SLAM will seed the selection process with both the current keyframe and the virtual keyframe at near-future. It will then seek for the subgraph maximizing the conditioning of current and the near-future estimates. Once found, the subgraph without the virtual keyframe defines the local BA problem to solve, whose size is compatible to the targeted time budget and whose structure is optimized for the predicted camera trajectory.

Based on the above implementation, the active *Good Graph* algorithm modification for VSLAM has similar properties to the active *Good Features* (GF) matching algorithm [9]. In the GF system, before actively establishing which map points to match against the current keyframe, there first exists a test to establish whether active matching should be instantiated and how many matches should be sought, followed by a fast selection mechanism. Adaptively enabling or disabling the *Good Features* component based on the runtime or data-driven properties of the SLAM algorithm provided a unique approach to active matching by triggering the process only when necessary. When triggered, the size of the subset selected was determined by a desired feature matching quantity. In doing so, it was one of the first active matching approaches to save time, in the sense that the combined time cost of the active matching and the reduced size pose optimization was lower than that of the full size pose optimization. Given that the *Good Graph* active selection mechanism has a similar design

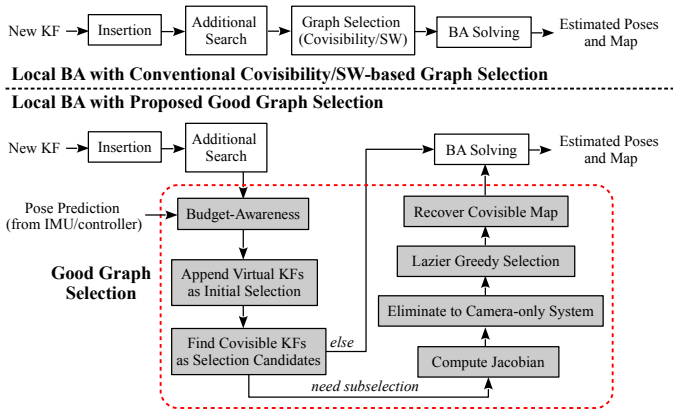


Fig. 6. Pipelines of local BA in VSLAM back-end. **Top**: conventional local BA pipeline, where the graph to be optimized is determined using heuristics such as covisibility or sliding-window (SW). **Bottom**: local BA pipeline with the proposed *Good Graph* selection integrated (shaded boxes), where the graph is determined using *Good Graph* algorithm when a smaller subgraph is desired per budget-awareness, i.e., $k < m$.

approach, the properties associated to the front-end processing of *Good Features* SLAM implementations should hold for the back-end processing of *Good Graph*, as the selection process is triggered only when the default local BA optimization size is too large to complete within the given budget. When triggered, an efficient selection process downsizes the local BA optimization to fit within the time budget without sacrificing estimation accuracy. Conversely, when there are no constraints, the process will take as much time as specified permissible. The adaptive compute design improves the properties of the SLAM pose estimation step by providing timely and accurate map estimates.

A visual description for the integration of the *Good Graph* algorithm into the local BA module of a VSLAM back-end is illustrated in Fig. 6. Though the incremental nature is exploited in the *LogDet* computation, the overall design of *Good Graph* algorithm has been implemented for batch BA, where each local BA is configured and solved independently. While batch BA is commonly used in BA-based VSLAM back-ends, a back-end with incremental BA should further improve cost-efficiency. In the future, a fully incremental design for *Good Graph* selection that couples with incremental BA solving is worth implementing.

VI. EXPERIMENTAL RESULTS

This section evaluates the performance of the proposed *Good Graph* algorithm in two different settings, open-loop and closed-loop. The open-loop setting is the more common benchmarking and evaluation approach, where the recorded data is re-played and processed. In this case, there is the option of processing with or without time constraints. The former option is chosen, which involves missed frames if the algorithm cannot process at the rates of the recorded signal, as the same would occur in real-world operation. The closed-loop setting is less commonly explored due to issues with reproducibility and ground-truth. Here, the use of simulation via ROS/Gazebo permits consistent and reproducible evaluation of SLAM systems, with the outcomes valid for

settings with similar visual and dynamic characteristics [1], [56], [57]. Closed-loop operation means that the SLAM pose estimate is used to generate the feedback control signal for a trajectory tracking module. Poor pose estimation will lead to poor trajectory tracking. In both evaluation settings, the *Good Graph* algorithm modification improves the cost-efficiency of BA and, consequently, the system performance.

A. *Good Graph* in Standalone VSLAM

Several *Good Graph* variants and baseline SLAM implementations inform the benchmarking analysis. Their descriptions and configurations are found here along with common experimental details.

1) *Good Graph* Implementation and Variants: The *Good Graph* algorithm was integrated into GF-ORB-SLAM (*GF* [9]), a BA-based, stereo VSLAM system based on ORB-SLAM. Relative to the canonical ORB-SLAM (*ORB* [24]), the *GF* modified front-end improves cost-efficiency through active (*map-to-frame*) feature matching. The back-ends of *GF* and *ORB* are identical: they both use covisibility to bound the local BA process. The *Good Graph* algorithm was integrated into the BA-based back-end of *GF*, dubbed *GF+GG*. Implementation of the *Good Graph* algorithm uses SLAM++ [53], which supports block matrix manipulation and incremental factorization. To simulate access to future poses in the open-loop setting, we add 10% white Gaussian error to the ground truth poses, and feed the noisy pose predictions to the budget-awareness module. Meanwhile, in the closed-loop setting, the budget-awareness module directly obtains future poses from the trajectory controller. The mapping between the local BA time budget and the desired subgraph size was estimated *a priori*, as per Fig. 5.

To assess *Good Graph* relative to other potential implementations, three GF-ORB-SLAM variants are included as evaluation baselines, with one of them being the standard GF-ORB-SLAM (*GF*). The second variant is a sliding-window strategy implemented for the BA back-end of *GF*, leading to a combined system denoted *GF+SW*. The third variant implements an aggressive state selection strategy based on covisibility: only the top- k covisible camera states get passed along to the local BA, while all covisible camera states are used in *GF*. It is referred to as *GF+CV*. For both *GF+SW* and *GF+CV* the problem size is bounded to 30 keyframes in local BA. All variants above are run as stereo only SLAM implementations (i.e., without using IMU data).

2) *Baseline Methods*: Five state-of-the-art visual(-inertial) SLAM systems with stereo camera support were included: *ORB* [24], *SVO* [3], VINS-Fusion [19], ICE-BA [20], and a visual-inertial implementation of MSCKF [4]. *ORB* stands for the canonical ORB-SLAM, which is a stereo visual-only SLAM system with feature-based front-end and BA-based back-end. *SVO* is a lightweight, visual-only odometry system with a direct front-end and a sliding window BA back-end. By skipping explicit feature extraction and matching, *SVO* is computationally lighter than the feature-based *ORB* and *GF* variants. VINS-Fusion, labeled *VIF*, is a visual-inertial SLAM system that performs sliding window BA in the back-end. ICE-BA, labeled *ICE*, is an incremental and sliding window BA

visual-inertial system. The visual-inertial implementation of MSCKF is dubbed *MSC*, and is included to also test a filter-based VSLAM. All three visual-inertial systems, namely *VIF*, *ICE* and *MSC*, track sparse optical flow in the front-end.

3) *Implementation / Experimental Setup*: Across the *Good Graph* variants and the baseline methods, a variety of back-end options are covered: covisibility and batch BA, sliding window and batch BA, sliding window and incremental BA, *Good Graph* and batch BA, and filter-based. A parameter sweep identified configuration parameters with good performance for these VSLAM systems.

General performance evaluation involves application of the test SLAM systems in *open-loop* with recorded sensor data. Again, *open-loop* refers to the fact that the estimation data does not impact actuation and therefore does not impact future sensor data. For the basic set of *open-loop* tests, the sensor signals were provided at their collection rate. This play-back rate would reflect SLAM estimation under normal conditions for the hardware used.

To assess the performance of VSLAM system under different computational limits, the same sensing data was provided at a higher frequency given by a multiple of the collection frequency, which we call *fast-mo*. This includes dropping or ignoring sensing data if the SLAM process has not yet completed from the prior sensor input cycle, in order to incorporate hard real-time constraints. Inspired by the idea of *slo-mo* in VSLAM benchmarking [1], *fast-mo* evaluation attempts to simulate different levels of computational limits and avoids the need to configure the evaluated VSLAM systems across multiple devices with different computational resources. In *fast-mo*, the VSLAM systems are configured on a single computer (Intel i7-7700K CPU, PassMark 2583 per core), but are evaluated using different rates of visual input data. VSLAM performance on a PC with 4x *fast-mo* give a rough upper bound of a method’s actual real-time performance on a 4-time slower device (with less cache, lower data throughput rate, lower transmission rate, etc.). Five levels of *fast-mo* speeds are evaluated, ranging from 1x to 5x. A low-power CPU can be simulated with 2x and 3x *fast-mo*, while an ARM SoC can be simulated with 4x and 5x *fast-mo* [58].

Since lower powered compute hardware is often enhanced by additional hardware-acceleration modules, an additional set of experiments was performed for the variants to simulate the effect of working with a hardware-accelerated front-end. This test set assesses the performance impact of the *Good Graph* local BA back-end when combined with co-computing modules. Rather than providing the raw video data, the implementations are given precomputed feature points. Doing so removes the overhead of the front-end feature extraction (i.e., from 16 ms to 3 ms per stereo frame). Performance of an actual VSLAM system consisting of hardware acceleration with *GF/GG* algorithmic improvements should fall between the regular *fast-mo* results and the precomputed results.

4) *Dataset and Evaluation Criteria*: The open-loop evaluation is based on the EuRoC benchmark [59], which contains 11 stereo-inertial sequences recorded in three different indoor environments. The performance of each VSLAM system is evaluated using the real-time pose tracking output. Real-time

pose tracking accuracy is measured by the *absolute root-mean-square error* (RMSE) [60] between the ground truth trajectory and the real-time VSLAM output from the pose estimation step, after conducting an *SE3* alignment (with no scale correction). Robustness of each VSLAM system is quantified by the number of successfully tracked sequences versus the total number of sequences. For each configuration (benchmark sequence, VSLAM system, *fast-mo* speed, with/without precomputing), a 10-run repeat was executed. Track failure is concluded when more than 40% of frames are not tracked successfully. Results were reported only if zero tracking failure occurred during the 10-run repeat. Otherwise, the results of the corresponding configuration were discarded since the VSLAM system output was not reliable.

Table V presents the open-loop *fast-mo* outcomes of different VSLAM methods on the EuRoC benchmark. For each sequence, the lowest RMSE values with the same category (defined by *fast-mo* speed and with/without precomputing) are highlighted in bold. The average RMSE values of each VSLAM method, across the columns, are listed in the right-most column, where those with more track loss than *GF+GG* are marked in parentheses. Table V is the source data for the analysis presented in the next two subsections.

B. Analysis of Good Graph Variants

The *GF* method and variants all performed well at the standard (1x) rate. On average, the back-end modifications preserved performance as determined by robustness (all methods tracked all sequences) and accuracy, with the *GF+GG* RMSE being equal to or lower than (within 5%) the *GF* version, as indicated by the last column in Table V. In these cases, there is usually sufficient time for the local BA process to influence pose estimation. As the *fast-mo* speed increases, the time allocation of the SLAM computation shrinks relative to the time between camera measurements, and the performance outcomes diverge. The *GF*, *GF+SW*, and *GF+CV* versions experience degraded robustness and cannot reliably track all sequences. At 4x *fast-mo* the *GF+GG* version starts to present reduced robustness (3 out of the 11 sequences has track failure). None of the methods track at 5x *fast-mo*. The ability of *GF+GG* to track through to 3x with no track loss shows that accelerating the back-end through prioritized and time-aware optimizations can enhance pose estimation through better optimized map points. With precomputed keypoints, *GF+GG* could be pushed to 4x rates with no track loss, and only fails on 2 sequences at 5x:Pre.

The *Good Graph* modification not only improves the overall outcomes, but it exhibits lower performance variation as a function of the *fast-mo* factor. Fig. 7 includes boxplots of the tracking accuracy outcomes on three EuRoC sequences. In each boxplot, the outcomes are grouped by *GF* variant methods; for each variant the boxes are ordered per *fast-mo* speed. The gray columns stand for configurations with track loss. The *GF+GG* version has more consistent outcomes on *MH 03* and *VI 02 med* (first 2 columns). Though the variation of tracking accuracy increases for *VI 03 diff*, it has the most success across the *fast-mo* speeds. None of the other variants

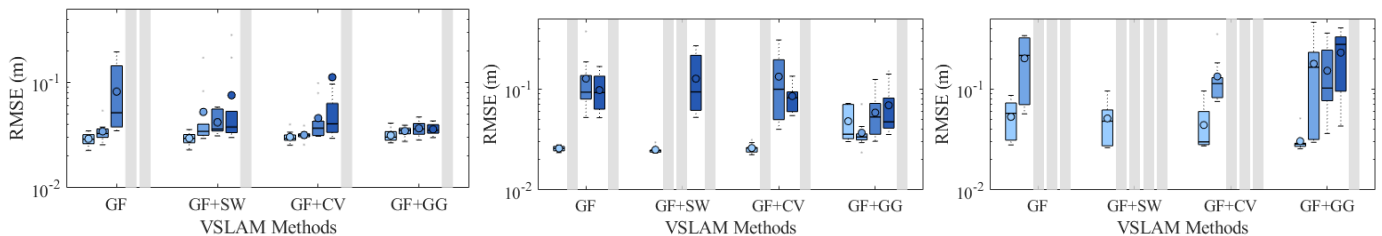


Fig. 7. *Fast-mo* results of GF variants without precomputed keypoints, on three EuRoC sequences: *MH 03 med* (left), *VI 02 med* (middle) and *VI 03 diff* (right). See text for plot details. *GF+GG* shows advantage over other GF variants in terms of both track success and RMSE.

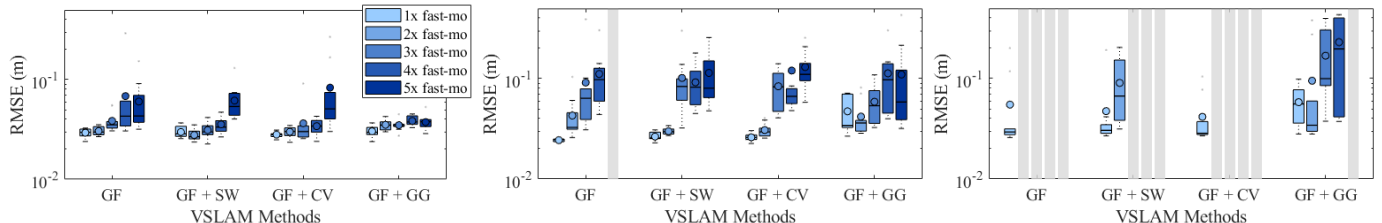


Fig. 8. *Fast-mo* results of GF variants with precomputed keypoints, on the same three sequences. Compared with Fig. 7, track failures happened less because of the removal of the front-end bottleneck. The *GF+GG* variant addresses the cost-efficiency issue of BA-based back-end nicely, as it tracks on more *fast-mo* settings (especially $\geq 3x$) than the rest, while keeping lower or similar RMSE.

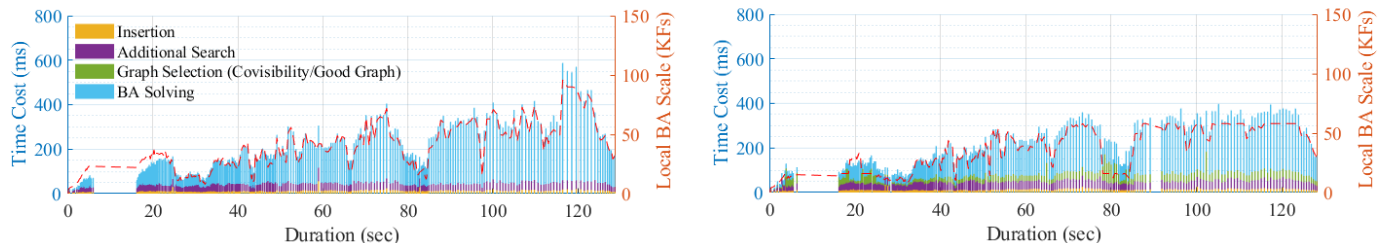


Fig. 9. Time cost breakdowns (left y -axis) and graph size (right y -axis) of local BA specification and optimization on *MH 03 med*, at $2x$ *fast-mo*. No local BA is triggered between 7 sec and 15 sec since the camera remains static. **Left:** *GF* uses all covisible keyframes in the local BA based on the *ORB* implementation. **Right:** *GF+GG* selects and optimizes the good subgraph in local BA.

can track beyond $2x$ *fast-mo* for *VI 03 diff*. To factor out the front-end bottleneck in *fast-mo* evaluation, boxplots of outcomes with precomputed keypoints are provided in Fig. 8. Although track loss happened less for the *GF* variants on *MH 03* and *VI 02 med*, *GF+GG* stands out, with consistent tracking accuracy (especially on $5x$ *fast-mo*). Interestingly, the pre-computing doesn't improve the track success of other *GF* variants on *VI 03 diff*, which indicates the bottleneck of this sequence is on the BA-based back-end, and that it is largely resolved with *GF+GG*.

To demonstrate the functionality of *Good Graph* in practice, Fig. 9 provides a time cost breakdown versus time of the BA back-end components for a $2x$ *fast-mo* instance. The red curve corresponds to the right-hand y -axis in the figure, which is the target local BA size versus time. The *GF* version does not modify the *ORB* local BA calculations, thus they vary as a function of the covisible keyframes, which adds variability to the local BA solver time. The *GF+GG* version bounds the local BA solver time by adaptively choosing the quantity of keyframes used in the local BA optimization. During the first 60 seconds of exploration both methods have similar time cost profiles. Afterwards, the time cost distribution of *GF+GG* is 265.6 ± 77.5 ms versus 259.8 ± 95.6 ms for the *GF* baseline. These statistics are consistent with the earlier BA-

only evaluation of *Good Graph*. It tends to select a larger local BA problem in terms of map points for the given target set of camera poses (as determined by an upper limit on compute time). Achievement of the compute bound is indicated by the lower variance (77.5 vs 95.6). Without this component, the local BA problem size and its numerical solution time fluctuates more. Further confirmation arises from examining the L_2 norm of the derivative of the two curves (the local BA problem size and compute time versus frame). The *GF* baseline has norms 164 keyframes/sec and 0.8 sec/sec, while *GF+GG* has norms 118 keyframes/sec and 0.6 sec/sec. The latter two quantities are lower than *GF* values by 27-28%, indicating less fluctuation of the constructed local BA problem versus time.

C. Analysis Relative to Baseline Methods

According to Table V, the two visual-inertial systems with sliding window BA (*ICE* and *VIF*) had significantly higher RMSEs for 1-3x *fast-mo* factors, and failed to track since $4x$ *fast-mo*. The two lightweight systems, direct *SVO* and filter-based *MSC*, were robust under all five *fast-mo* speeds but with high RMSEs. The *GF+GG* system consistently had one of the lowest RMSEs with full tracking success for 1-3x *fast-mo*. The track failure of *GF+GG* running on 4-5x *fast-mo* is partially

TABLE V
RMSE (M) ON EUROC STEREO SEQUENCES FOR STANDARD COMPUTER

Cfg	Methods	Sequences											Avg.
		MH 01	MH 02	MH 03	MH 04	MH 05	VI 01	VI 02	VI 03	V2 01	V2 02	V2 03	
1x; Pre	GF	0.025	0.019	0.029	0.109	0.064	0.035	0.024	0.055	0.043	0.040	0.228	0.061
	GF + SW	0.023	0.018	0.030	0.104	0.064	0.036	0.026	0.047	0.046	0.040	0.183	0.056
	GF + CV	0.021	0.018	0.028	0.113	0.061	0.036	0.026	0.042	0.046	0.042	0.160	0.054
	GF + GG	0.024	0.018	0.030	0.110	0.070	0.036	0.047	0.058	0.043	0.046	0.173	0.060
1x	GF	0.023	0.018	0.029	0.119	0.066	0.036	0.026	0.053	0.042	0.046	0.186	0.059
	GF+SW	0.023	0.018	0.029	0.094	0.062	0.036	0.025	0.051	0.046	0.045	0.220	0.059
	GF+CV	0.021	0.019	0.030	0.115	0.065	0.036	0.026	0.044	0.046	0.046	0.194	0.058
	GF+GG	0.027	0.019	0.031	0.107	0.073	0.036	0.048	0.030	0.042	0.036	0.161	0.056
	ORB	0.030	0.025	0.032	0.166	0.089	0.037	0.034	0.310	0.049	0.083	0.304	0.105
	MSC	-	0.139	0.239	0.273	0.245	0.092	0.105	0.168	0.063	0.136	1.290	(0.275)
	ICE	0.115	0.075	0.119	0.233	0.237	0.066	0.096	0.153	0.115	0.101	0.175	0.135
	VIF	1.152	1.324	1.490	2.243	2.310	0.345	0.350	0.533	0.474	0.373	0.268	0.987
SVO	0.126	0.102	0.242	1.942	0.292	0.092	0.269	0.359	0.159	0.236	2.471	0.572	
2x; Pre	GF	0.025	0.019	0.030	0.107	0.064	0.060	0.043	-	0.045	0.064	0.144	(0.060)
	GF+SW	0.028	0.019	0.028	0.132	0.067	0.036	0.030	0.090	0.042	0.057	0.206	0.067
	GF+CV	0.028	0.020	0.030	0.125	0.069	0.037	0.031	-	0.043	0.052	0.167	(0.060)
	GF+GG	0.024	0.020	0.035	0.138	0.079	0.036	0.042	0.095	0.043	0.049	0.150	0.065
2x	GF	0.028	0.021	0.034	0.133	0.083	0.037	-	0.202	0.044	0.071	0.113	(0.077)
	GF+SW	0.030	0.021	0.052	0.108	0.085	0.036	-	-	0.046	0.068	0.117	(0.062)
	GF+CV	0.025	0.022	0.032	-	0.099	0.036	-	0.134	0.048	0.058	0.123	(0.064)
	GF+GG	0.024	0.022	0.035	0.118	0.084	0.036	0.037	0.178	0.041	0.051	0.194	0.075
	ORB	0.032	0.026	0.059	0.190	0.097	0.037	-	-	-	0.174	-	(0.088)
	MSC	-	0.169	0.228	0.244	0.283	0.102	0.127	0.189	0.077	0.150	-	(0.174)
	ICE	0.116	0.074	0.147	0.276	0.249	0.062	0.094	0.146	0.113	0.102	0.299	0.152
	VIF	1.153	1.324	1.505	2.255	2.316	0.345	0.350	0.552	0.467	0.374	0.264	0.991
SVO	0.127	0.106	0.220	2.081	0.438	0.097	0.292	0.409	0.186	0.260	2.391	0.601	
3x; Pre	GF	0.033	0.021	0.039	0.155	0.083	0.038	0.091	-	0.043	0.088	0.158	0.075
	GF+SW	0.029	0.022	0.031	0.138	0.083	0.045	0.102	-	0.042	-	0.195	(0.076)
	GF+CV	0.026	0.023	0.036	0.145	0.072	0.052	0.084	-	0.045	-	0.159	(0.071)
	GF+GG	0.023	0.021	0.035	0.156	0.087	0.036	0.059	0.169	0.042	0.059	0.198	0.080
3x	GF	0.031	0.024	0.082	0.174	0.090	0.040	0.127	-	0.048	0.093	-	0.079
	GF+SW	0.033	0.022	0.042	0.151	0.099	0.038	-	-	0.050	-	0.153	(0.073)
	GF+CV	0.035	0.027	0.046	0.160	0.095	0.039	0.133	-	0.061	0.094	-	0.077
	GF+GG	0.027	0.023	0.037	0.154	0.098	0.037	0.059	0.152	0.048	0.059	0.169	0.078
	ORB	0.029	0.026	0.047	-	0.095	-	-	-	0.131	-	-	(0.066)
	MSC	-	0.151	0.274	-	0.329	0.108	0.136	0.230	0.078	0.158	-	(0.183)
	ICE	0.112	0.261	0.420	0.236	0.232	0.066	0.094	0.190	0.121	-	-	0.192
	VIF	1.029	1.042	1.476	2.273	2.313	0.320	0.347	0.549	0.434	0.365	0.262	0.946
SVO	0.117	0.117	0.282	1.872	0.447	0.094	0.293	0.339	0.220	0.399	2.514	0.609	
4x; Pre	GF	0.035	0.028	0.068	0.147	0.088	0.050	0.111	-	0.043	-	0.202	(0.086)
	GF+SW	0.037	0.025	0.035	0.166	0.089	0.039	0.092	-	0.048	-	0.144	(0.075)
	GF+CV	0.032	0.023	0.034	0.182	0.103	0.039	0.120	-	0.043	-	-	(0.072)
	GF+GG	0.027	0.023	0.038	0.161	0.082	0.036	0.113	0.231	0.045	0.063	0.202	0.093
4x	GF	-	0.022	-	0.189	0.123	-	0.098	-	0.065	-	-	(0.100)
	GF+SW	-	0.022	0.075	0.178	0.142	-	0.127	-	0.113	0.145	-	0.136
	GF+CV	-	0.023	0.112	0.201	0.115	-	0.085	-	0.081	-	-	(0.103)
	GF+GG	-	0.024	0.036	0.178	0.095	-	0.069	0.230	0.047	0.064	-	0.093
	ORB	0.031	0.024	-	0.210	0.118	0.039	0.105	-	0.210	0.101	-	0.105
	MSC	-	0.223	0.262	1.319	0.317	0.149	0.162	-	0.096	0.150	-	0.335
	ICE	0.096	0.808	-	0.258	0.225	0.070	-	-	0.113	-	-	(0.262)
	VIF	-	-	-	-	-	-	-	-	-	-	-	-
SVO	0.122	0.114	0.457	2.173	0.400	0.093	0.445	0.485	0.183	0.493	2.311	0.661	
5x; Pre	GF	0.039	0.025	0.060	0.181	0.104	0.051	-	-	0.078	0.112	0.200	0.094
	GF+SW	0.046	0.024	0.062	0.182	0.117	0.043	0.114	-	0.048	0.095	0.206	0.094
	GF+CV	0.048	0.025	0.083	0.202	0.112	0.048	0.130	-	0.067	0.132	-	0.094
	GF+GG	0.028	0.026	0.037	0.173	0.100	0.038	0.110	-	0.048	0.067	-	0.070
5x	GF	-	-	-	-	-	-	-	-	-	-	-	-
	GF+SW	-	-	-	-	-	-	-	-	-	-	-	-
	GF+CV	-	-	-	-	-	-	-	-	-	-	-	-
	GF+GG	-	-	-	-	-	-	-	-	-	-	-	-
	ORB	-	-	-	-	-	-	-	-	-	-	-	-
	MSC	-	-	0.361	-	0.817	0.129	0.178	-	-	0.259	1.341	0.514
	SVO	0.106	0.112	0.446	1.883	0.355	0.094	0.524	0.475	0.216	0.518	2.363	0.645

TABLE VI
RMSE (M) ON EUROC STEREO SEQUENCES FOR AN EMBEDDED DEVICE

Cfg	Methods	Sequences											Avg.
		MH 01	MH 02	MH 03	MH 04	MH 05	VI 01	VI 02	VI 03	V2 01	V2 02	V2 03	
1x: Pre	GF	-	0.055	0.054	0.129	-	0.049	-	-	0.049	-	-	(0.067)
	GF+SW	-	0.032	0.113	-	-	0.044	-	-	0.063	0.105	-	(0.071)
	GF+CV	-	-	0.057	0.174	-	0.045	0.112	-	0.052	0.097	-	(0.089)
	GF+GG	0.036	0.025	0.061	0.141	0.097	0.038	0.122	-	0.042	0.092	-	0.077
1x	GF	-	-	-	-	-	0.048	-	-	-	-	-	(0.048)
	GF+SW	-	-	-	-	-	0.050	-	-	-	-	-	(0.050)
	GF+CV	-	-	-	-	-	0.066	-	-	-	-	-	(0.066)
	GF+GG	0.037	-	0.059	0.176	0.140	0.039	-	-	0.048	0.084	-	0.083
	ORB	-	-	-	-	-	-	-	-	-	-	-	-
	MSC	-	0.136	0.249	0.228	0.355	0.087	0.105	0.179	0.065	0.119	0.970	0.249
	ICE	0.100	0.320	-	0.247	0.224	0.067	0.107	-	-	-	-	(0.177)

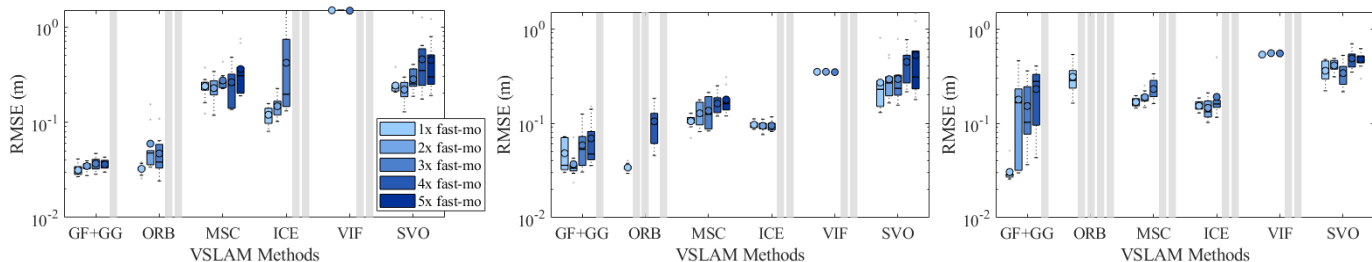


Fig. 10. *Fast-mo* results of *GF+GG* and state-of-the-art visual(-inertial) SLAM baselines, on the same three sequences (*MH 03*, *VI 02*, *VI 03*).

due to the front-end bottleneck, as seen by the full tracking at 4x:Pre and 9 of 11 tracking at 5x:Pre. With precomputing, the error rates of *GF+GG* are at least 7 times lower than *SVO*.

To visualize performance progression as a function of *fast-mo* settings, Fig. 10 depicts box plots of the tracking accuracy outcomes for *GF+GG* and the baselines. The proposed *GF+GG* has the best average tracking accuracy in all except for 2 cases: for 1x on *VI 02 med* where it is slightly worse than *ORB*, and for 2x on *VI 03 diff* where it's slightly worse than *ICE*. In both cases the differences are negligible relative to the range of RMSE values across all of the methods. Moreover, *GF+GG* is the only BA-based VSLAM that tracks from 1x to 4x *fast-mo* on all 3 example sequences.

This study shows that by adding a compute aware local BA back-end to the accelerated front-end *GF* of ORB-SLAM further improves the run-time performance properties of SLAM system. *GF* demonstrated improved performance relative to published baselines [9], while *GG* provides additional robustness to computational resources and/or timing constraints. The performance degradation of *GF+GG* is relatively graceful from 1x *fast-mo* to 4x *fast-mo*.

D. Good Graph on Embedded Device

To confirm that the predicted outcomes of *fast-mo* (especially 4x and 5x) agree with the actual results on the equivalent low-power device, we ran the experiments using EuRoC sequences on an embedded device, Nvidia Jetson TX2 with an ARM SoC (Cortex A57) and 7.5W of power consumption. Evaluation results of *GF+GG*, alongside with three *GF* variants and three baseline methods (*ORB*, *MSC*,

and *ICE*), are summarized at Table VI. Due to hardware compatibility issues, the *VIF* and *SVO* baselines were dropped.

In terms of robustness and low-cost, the light-weight visual-inertial *MSC* stands out with only one tracking failure. The integration of inertial information assists the data association component. Nevertheless, the RMSE achieved by *MSC* was high, mostly due to the drift accumulation of the filter with a short time sliding window. The visual-only *GF+GG* is not as robust as *MSC*, but does exhibit a lower RMSE than both visual-inertial systems *MSC* and *ICE*. When compared to the *GF* variants, *GF+GG* shows improved robustness as it tracked 7 of the sequences, versus 1 for the variants. Performance of the embedded *GF+GG* is closest to the 4x *fast-mo* case.

Using precomputed feature points, *GF+GG* tracks 9 of the sequences and has a slightly lower RMSE (by 7%). The outcomes are similar to *GF+GG* for the 5x:Pre *fast-mo* case. The variants track more than their 1x counterparts, but still less than *GF+GG*. The clear performance improvement from *GF* to *GF+GG* suggests that the *Good Graph* modification compensates for BA back-end bottlenecks by directing available computational resources towards BA sub-graph components helpful to the front-end. Additional parameter tuning with an FPGA-based front-end, and possibly the incorporation of inertial signals, should resolve the four failure cases in *GF+GG* 1x (or the two in 1x:Pre), and provide a low-drift SLAM system for small scale robotic systems or localization and mapping devices.

E. Good Graph in VSLAM-based Closed-loop Navigation

In practical applications such as closed-loop navigation, VSLAM would be a subsystem within an autonomous nav-

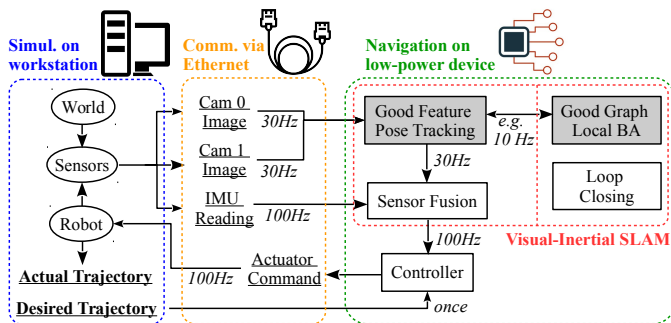


Fig. 11. Overview of the closed-loop navigation system, in which $GF+GG$ is argued into a loosely-coupled visual-inertial SLAM system with inertial fusion. Other visual(-inertial) SLAM systems were easily plugged into the navigation system for comparison.

igation system. The envisioned role of VSLAM for mobile robots is to provide pose estimates when navigating through environments. Especially in cases where GPS positioning is less reliable or unavailable. The VSLAM subsystem provides robot pose estimates to other autonomy components, which require pose for feedback or for processing measurements. Consequently, closed-loop navigation performance will be affected by VSLAM subsystem performance relative to robustness, accuracy, and latency. This section’s investigation will show that enhancing VSLAM-based state estimation with the *Good Graph* algorithm improves navigation performance. The combination of the *Good Graph* back-end and the low-latency *Good Feature* front-end, $GF+GG$, will be evaluated. The *Good Graph* modification improves the cost-efficiency of local BA, and increases the quality of map points available for pose tracking. The budget-awareness module of *Good Graph* uses the trajectory to track as predicted future poses, with which it establishes a time compatible local BA budget.

1) *Closed-loop Navigation System Design*: The closed-loop navigation benchmarking system introduced in [57] is extended to evaluate the proposed Good-Graph algorithm. The block diagram in Fig. 11 provides a visual overview of the system. While the original system [57] implemented the simulation and navigation stack on a single workstation, here we perform a hardware-in-the-loop computing experiment. The processes that would be performed on a robot are off-loaded to a low-power compute device, which includes the VI-SLAM, sensor fusion, and trajectory controller modules. The workstation and the low-power device communicate via Ethernet. The top row of the figure depicts the two devices and their connectivity. The bottom row depicts further details of the systems, with the left-most part representing the ROS/Gazebo simulation and the middle part the transmitted signals and their rates. The right-most part depicts the three major navigation subsystems: 1) a visual SLAM subsystem taking stereo vision data to generate sparse yet accurate state estimates; 2) an EKF-based sensor fusion subsystem [61] taking both sparse visual estimates and high-rate IMU readings for high-rate and accurate positioning; and 3) a PID position controller [62] taking the high-rate output from the sensor fusion subsystem and generating actuator commands.

2) *Baseline Methods*: The canonical ORB-SLAM (*ORB*) [55] and the front-end-improved *GF* variant [9] serve as com-

parison baselines within the same solution class. Additional baseline methods using other SLAM approaches include three of the four visual(-inertial) SLAM systems from the previous standalone VSLAM evaluation: 1) filter-based, visual-inertial *MSC* [4], 2) visual-inertial *VIF* with sliding window BA [19], and 3) visual-only *SVO* with sliding window BA [3]. *ICE* is not included due to the lack of ROS support.

3) *Simulation Setup*: The simulation setup is a virtual office world of dimensions $20\text{m} \times 20\text{m}$ depicted in Fig. 12. The virtual world is based on the floor-plan of an actual office, with texture-mapped surfaces [57]. The walls are placed 1m above the ground plane since collision checking and path planning is outside the scope of this evaluation; we wish to avoid this as a factor influencing the outcomes. The differential drive robot TurtleBot2 [63] is commanded to track reference trajectories within the office world. Mounted to the robot are a 30fps stereo camera with an 11cm baseline and an IMU placed at the base of TurtleBot. Two commonly-used IMUs are simulated: a high-end ADIS16448 and a low-end MPU6000. Data streams from both the stereo camera and IMU are input to the visual(-inertial) SLAM which then outputs $SE(3)$ state estimates. The trajectory tracker [62] uses the $SE(2)$ subspace of the $SE(3)$ estimate to track the desired path.

4) *Experiment Details*: The navigation benchmark consists of six test paths as illustrated in Fig. 13, each with different characteristics [57]. The first two paths are short ($\sim 50\text{m}$), with few to no re-visits. The third and fourth paths are medium length ($\sim 120\text{m}$) with many to few re-visits. The last two paths are long ($\sim 240\text{m}$) with many re-visits. All paths start at the world origin where the robot is placed (top-left corner of Fig. 12). Three desired linear velocities are tested: 0.5m/s, 1.0m/s, and 1.5m/s. Each closed-loop navigation test configuration (desired path, desired linear velocity, VI-SLAM method, and IMU) is run 5 times, with the average performance outcomes presented in the case of no track failures. Configurations with at least one track failure are thrown out.

Gazebo simulation and graphics rendering occurs in real-time on an Intel Xeon E5-2680 dual-CPU workstation (passmark score 1661 per thread). The closed-loop navigation computation includes VSLAM, visual-inertial fusion, and feedback control. These processes occur on a laptop with a low-power Intel Core i7-8550U CPU (single-thread Passmark score of 2140 and power consumption of 15W). For reference, most published closed-loop navigation systems [4], [64]–[69] employ Intel NUC whose CPU scores between 1900–2300 per thread. There is a transport delay of approximately 30 ms for the sensor signals between the simulation workstation and the navigation laptop.

The navigation performance metric is the root-mean-square error (RMSE) between the desired path and the actual path, averaged over the 5-run repeats. In addition to a 40% track loss limit, any trajectory with average RMSE over 10m is considered to be a navigation failure and the entire 5-run test case is omitted (the dashes). The full results of closed-loop navigation discussed here with all 6 visual(-inertial) SLAM systems are also available online [30].

5) *Navigation Results on Low-Power Laptop*: Tables VII and VIII provide the quantitative outcomes for navigation

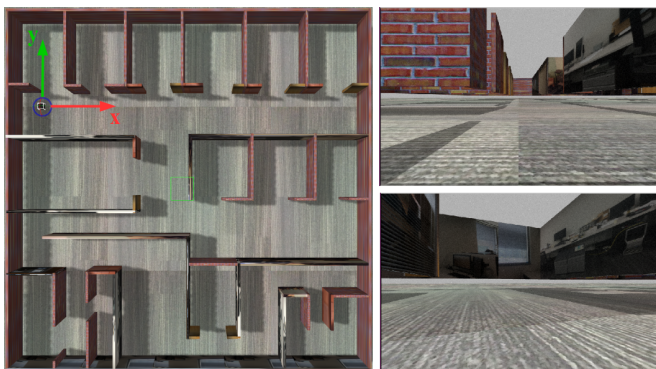


Fig. 12. The virtual office world. **Left:** Top-down view. The robot starts at the top-left corner, facing the long corridor. **Right:** Example images captured by on-board stereo camera (left camera).

TABLE VII
NAVIGATION ERROR (RMSE; IN M), WITH HIGH-END IMU ADIS16448

Vel.	Meth.	Sequences						Avg.
		<i>s1</i>	<i>s2</i>	<i>m1</i>	<i>m2</i>	<i>l1</i>	<i>l2</i>	
0.5 m/s	GF	0.12	0.12	0.18	0.12	0.22	-	(0.15)
	GF+GG	0.14	0.11	0.21	0.14	0.23	0.32	0.19
	ORB	0.16	0.82	-	0.32	-	5.29	(1.65)
	MSC	0.34	0.35	0.50	0.62	0.56	0.58	0.49
	VIF	-	0.64	-	-	-	-	(0.64)
	SVO	2.00	-	-	-	-	-	(2.00)
1.0 m/s	GF	-	0.12	0.24	0.20	0.42	0.36	(0.27)
	GF+GG	0.14	0.11	0.23	0.19	0.33	0.46	0.24
	ORB	0.24	0.17	2.40	-	-	-	(0.94)
	MSC	0.26	0.45	0.53	0.67	0.85	0.87	0.61
	VIF	5.59	-	-	0.88	-	-	(3.24)
	SVO	1.06	8.49	-	-	-	-	(4.78)
1.5 m/s	GF	0.23	0.19	0.65	0.21	0.33	0.44	0.34
	GF+GG	0.21	0.17	0.26	0.23	0.39	0.27	0.26
	ORB	0.48	0.36	0.40	0.82	0.58	0.82	0.58
	MSC	-	0.39	0.52	0.51	0.76	-	(0.55)
	VIF	5.40	7.80	0.58	-	-	-	(4.59)
	SVO	0.54	1.52	-	-	-	-	(0.88)

performance with the high-end and low-end IMUs, respectively. Similar to Table VI, the lowest RMSEs with the same category (defined by desired path, desired linear velocity, and IMU) are highlighted in bold. On the rightmost column the average RMSEs are summarized, where the average numbers in parentheses indicate more track loss than *GF+GG*. Across the three speed settings, there were 18 sequences tested per IMU case. *SVO*, *VIF*, and *ORB* were the least robust for both IMU cases. For the high-end IMU, there were 13, 12, and 5 tracking failures, respectively. For the low-end IMU, there were 14, 17, and 9 failures. Prior evaluation has shown *SVO* to be quite robust [9], [57], however in this case the data transport delay combined with the typically large pose estimation error of *SVO* undermines stable operation. In what follows, we will focus on the implementations with better tracking success.

Of the remaining methods with low tracking failure counts, the *GF+GG* variant had only 1 track failure over the 36 tests, while *GF* had 3, and *MSC* had 4. Furthermore, *GF+GG* had more consistent error outcomes under the different desired

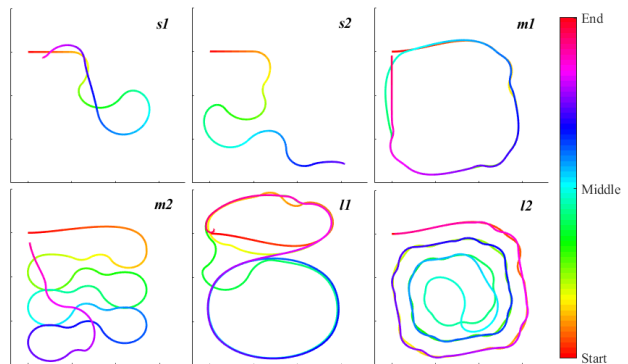


Fig. 13. The 6 desired paths used in closed-loop navigation experiments (best viewed in color). The color-coding indicates path progression (see colorbar).

TABLE VIII
NAVIGATION ERROR (RMSE; IN M), WITH LOW-END IMU MPU6000

Vel.	Meth.	Sequences						Avg.
		<i>s1</i>	<i>s2</i>	<i>m1</i>	<i>m2</i>	<i>l1</i>	<i>l2</i>	
0.5 m/s	GF	0.13	0.14	1.02	0.36	0.36	0.55	0.43
	GF+GG	-	0.17	0.36	0.35	0.63	0.66	0.43
	ORB	0.25	1.18	-	-	-	-	(0.72)
	MSC	0.32	0.34	0.54	0.43	0.84	0.63	0.52
	VIF	-	-	0.53	-	-	-	(0.53)
	SVO	0.17	-	-	-	-	-	(0.17)
1.0 m/s	GF	0.17	0.15	0.21	0.14	0.42	0.34	0.24
	GF+GG	0.17	0.19	0.26	0.48	0.39	0.49	0.33
	ORB	0.22	0.18	0.44	-	-	-	(0.28)
	MSC	-	0.41	0.43	0.39	0.56	0.62	(0.48)
	VIF	-	-	-	-	-	-	-
	SVO	0.98	-	-	-	-	-	(0.98)
1.5 m/s	GF	-	0.25	0.63	0.17	0.44	0.40	(0.38)
	GF+GG	0.20	0.19	0.29	0.20	0.35	0.45	0.28
	ORB	0.43	0.43	0.36	1.02	-	-	(0.56)
	MSC	0.31	0.36	0.59	0.51	0.66	-	(0.53)
	VIF	-	-	-	-	-	-	-
	SVO	0.79	5.32	-	-	-	-	(3.06)

velocities when compared to *GF* and *MSC* for both IMU cases. For the high-end IMU, the average error of *GF+GG* increased from 0.19 to 0.26 RMSE(m), whereas the *GF* RMSE went from 0.15 to 0.34, and the *MSC* RMSE went from 0.49 to 0.55. A roughly similar trend for the average RMSE range holds for the low-end IMU case, though performance is not strictly increasing as a function of speed, which suggests that the magnitude of the IMU error and the nominal pose difference influences RMSE outcomes. Outside of *GF+GG*, the best performing method is *GF*. The inclusion of the *Good Graph* component improves tracking robustness and smooths out performance variation, though the *GF+GG* does lead to a small increase in RMSE error relative to the best performing statistics for *GF* alone. Across all of the sequences *GF+GG* has mean and standard deviation of 0.285 ± 0.140 while *GF* has 0.304 ± 0.197 (for reference, *MSC* statistics are 0.522 ± 0.162). While consolidating all of the data aggregates different scenarios, the improved outcome consistency is an indicator of algorithm insensitivity to the nuisance factors associated to the

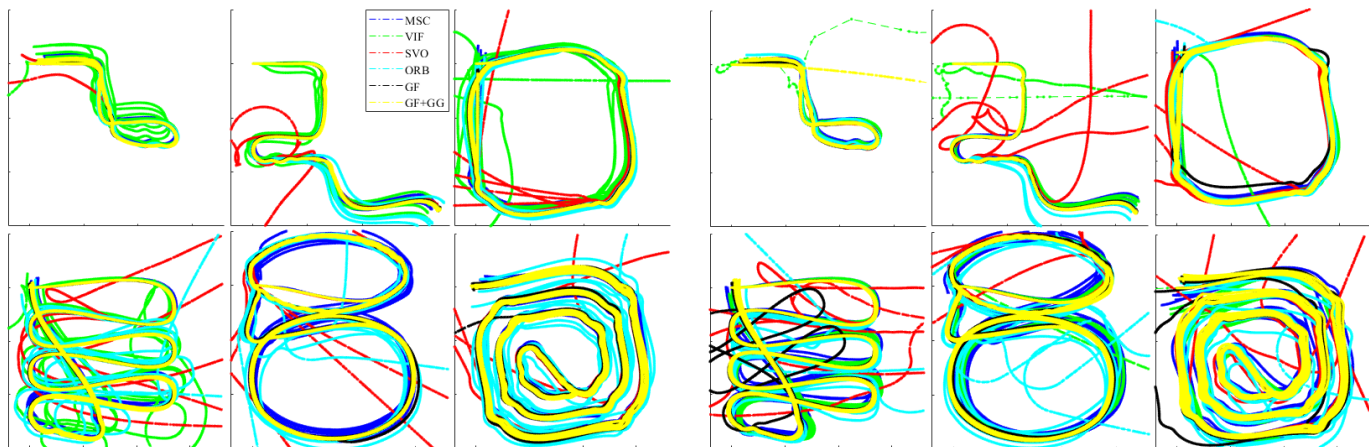


Fig. 14. Trajectories the robot traveled for each desired path, with a desired velocity of 0.5m/s. The trajectories are color-coded by method. **Left:** simulated with a high-end ADIS16448 IMU model. **Right:** simulated with a low-end MPU6000 IMU model.

different scenarios (path type, vehicle speed, and IMU noise level). The insensitivity demonstrates that adaptively adjusting the SLAM back-end according to runtime characteristics and solve-time needs does improve overall performance.

To qualitatively visualize the impact of these different RMSE error statistics, Fig. 14 depicts the actual trajectories traveled by the robot with 0.5m/s desired linear velocity, across the different SLAM implementations. The algorithms are color-coded with all five runs plotted per case tested. Trajectories leaving the plot bounds are clipped, thus worst case performance for some methods (*SVO*, *VIF*) is not completely visualized. *SVO* and *VIF* trajectories are completely decorrelated from the desired trajectories for many of the cases, which is an extreme form of track loss. *ORB* and *GF* have similar problems for a couple of cases. The high track error of *MSC* and *ORB* is visible for some of the cases as shifted or warped versions of the target trajectories, or as lateral offsets of the trajectory versus the reference one. The traveled and target trajectories do not agree but are still correlated. Thicker or multiple spread trajectories within a plot are further indications of high tracking variance. Fan out of the terminal state is an indication of pose estimation drift. Visually, *GF+GG* has the most consistent outcomes of the methods as established by the quantitative performance statistics.

VII. CONCLUSION

This paper describes the *Good Graph* modification, which improves the cost-efficiency of BA-based VSLAM back-ends under computational or timing limits. An efficient algorithm has been developed to select size-reduced graphs to be optimized in the local BA thread based on condition preservation. The desired size of the *Good Graph* is determined on-the-fly with budget-awareness. The *Good Graph* algorithm is evaluated in two example scenarios: 1) VSLAM as a standalone system, and 2) VSLAM as a part of closed-loop navigation system. The general BA results suggest that the *Good Graph* algorithm preserves the accuracy of 3D reconstruction while reducing the compute time, or the compute time per point processed. VSLAM evaluations are conducted under a variety of

computational limits. Analysis of the results demonstrate that the *Good Graph* algorithm successfully addresses compute and time cost awareness for BA-based back-ends, which improves VSLAM performance when there is performance loss based on compute or time constraints. For practical applications such as closed-loop navigation, the *Good Graph* algorithm enables accurate and compute-aware VSLAM, whose properties improve closed-loop navigation performance. As a general purpose modification to the BA back-end, *Good Graph* should apply to other SLAM methods besides ORB-SLAM. Open sourced code facilitates translation to these implementations [29].

REFERENCES

- [1] W. Ye, Y. Zhao, and P. A. Vela, "Characterizing SLAM benchmarks and methods for the robust perception age," *Workshop on Dataset Generation and Benchmarking of SLAM Algorithms for Robotics and VR/AR at the IEEE International Conference on Robotics and Automation*, 2019.
- [2] J. Delmerico and D. Scaramuzza, "A benchmark comparison of monocular visual-inertial odometry algorithms for flying robots," *IEEE International Conference on Robotics and Automation*, vol. 10, p. 20, 2018.
- [3] C. Forster, Z. Zhang, M. Gassner, M. Werlberger, and D. Scaramuzza, "SVO: Semidirect visual odometry for monocular and multicamera systems," *IEEE Transactions on Robotics*, vol. 33, no. 2, pp. 249–265, 2017.
- [4] K. Sun, K. Mohta, B. Pfrommer, M. Watterson, S. Liu, Y. Mulgaonkar, C. J. Taylor, and V. Kumar, "Robust stereo visual inertial odometry for fast autonomous flight," *IEEE Robotics and Automation Letters*, vol. 3, no. 2, pp. 965–972, 2018.
- [5] C. Cadena, L. Carlone, H. Carrillo, Y. Latif, D. Scaramuzza, J. Neira, I. Reid, and J. J. Leonard, "Past, present, and future of simultaneous localization and mapping: Toward the robust-perception age," *IEEE Transactions on Robotics*, vol. 32, no. 6, pp. 1309–1332, 2016.
- [6] M. Quigley, K. Mohta, S. S. Shivakumar, M. Watterson, Y. Mulgaonkar, M. Arguedas, K. Sun, S. Liu, B. Pfrommer, V. Kumar *et al.*, "The open vision computer: An integrated sensing and compute system for mobile robots," in *IEEE International Conference on Robotics and Automation*, 2019, pp. 1834–1840.
- [7] R. Liu, J. Yang, Y. Chen, and W. Zhao, "eSLAM: An energy-efficient accelerator for real-time ORB-SLAM on FPGA platform," in *Design Automation Conference*, 2019, pp. 193:1–193:6.
- [8] B. Nagy, P. Foehn, and D. Scaramuzza, "Faster than FAST: GPU-accelerated frontend for high-speed vio," *arXiv preprint arXiv:2003.13493*, 2020.
- [9] Y. Zhao and P. A. Vela, "Good feature matching: Towards accurate, robust VO/VSLAM with low latency," *IEEE Transactions on Robotics*, vol. 36, no. 3, pp. 657–675, 2020.

- [10] C. Wu, S. Agarwal, B. Curless, and S. Seitz, "Multicore bundle adjustment," in *IEEE Conference on Computer Vision and Pattern Recognition*, 2011, pp. 3057–3064.
- [11] S. Choudhary, S. Gupta, and P. Narayanan, "Practical time bundle adjustment for 3D reconstruction on the GPU," in *European Conference on Computer Vision*, 2010, pp. 423–435.
- [12] R. Hänsch, I. Drude, and O. Hellwich, "Modern methods of bundle adjustment on the GPU," *ISPRS Annals of Photogrammetry, Remote Sensing & Spatial Information Sciences*, vol. 3, no. 3, 2016.
- [13] S. Qin, Q. Liu, B. Yu, and S. Liu, " π -BA: Bundle adjustment acceleration on embedded FPGAs with co-observation optimization," in *IEEE 27th Annual International Symposium on Field-Programmable Custom Computing Machines*, 2019, pp. 100–108.
- [14] J. Ortiz, M. Pupilli, S. Leutenegger, and A. J. Davison, "Bundle adjustment on a graph processor," in *IEEE/CVF Conference on Computer Vision and Pattern Recognition*, 2020, pp. 2416–2425.
- [15] M. Li and A. I. Mourikis, "High-precision, consistent EKF-based visual-inertial odometry," *The International Journal of Robotics Research*, vol. 32, no. 6, pp. 690–711, 2013.
- [16] A. I. Mourikis and S. I. Roumeliotis, "A multi-state constraint Kalman filter for vision-aided inertial navigation," in *IEEE International Conference on Robotics and Automation*, 2007, pp. 3565–3572.
- [17] H. Strasdat, J. M. Montiel, and A. J. Davison, "Visual SLAM: why filter?" *Image and Vision Computing*, vol. 30, no. 2, pp. 65–77, 2012.
- [18] J. Engel, V. Koltun, and D. Cremers, "Direct sparse odometry," *IEEE Transactions on Pattern Analysis and Machine Intelligence*, vol. 40, no. 3, pp. 611–625, 2017.
- [19] T. Qin, P. Li, and S. Shen, "VINS-Mono: A robust and versatile monocular visual-inertial state estimator," *IEEE Transactions on Robotics*, vol. 34, no. 4, pp. 1004–1020, 2018.
- [20] H. Liu, M. Chen, G. Zhang, H. Bao, and Y. Bao, "ICE-BA: Incremental, consistent and efficient bundle adjustment for visual-inertial SLAM," in *IEEE Conference on Computer Vision and Pattern Recognition*, 2018, pp. 1974–1982.
- [21] V. Usenko, N. Demmel, D. Schubert, J. Stückler, and D. Cremers, "Visual-inertial mapping with non-linear factor recovery," *IEEE Robotics and Automation Letters*, vol. 5, no. 2, pp. 422–429, 2019.
- [22] A. Rosinol, M. Abate, Y. Chang, and L. Carlone, "Kimera: an open-source library for real-time metric-semantic localization and mapping," in *IEEE International Conference on Robotics and Automation*, 2020.
- [23] H. Strasdat, A. J. Davison, J. M. Montiel, and K. Konolige, "Double window optimisation for constant time visual SLAM," in *IEEE International Conference on Computer Vision*, 2011, pp. 2352–2359.
- [24] R. Mur-Artal and J. D. Tardós, "ORB-SLAM2: an open-source SLAM system for monocular, stereo and RGB-D cameras," *IEEE Transactions on Robotics*, vol. 33, no. 5, pp. 1255–1262, 2017.
- [25] R. Mur-Artal and J. D. Tardós, "Visual-inertial monocular SLAM with map reuse," *IEEE Robotics and Automation Letters*, vol. 2, no. 2, pp. 796–803, 2017.
- [26] C. E. M. Campos, R. Elvira, J. Rodríguez, J. M. M. Montiel, and J. D. Tardós, "ORB-SLAM3: An accurate open-source library for visual, visual-inertial and multi-map SLAM," *arXiv preprint arXiv:2007.11898*, 2020.
- [27] B. Mirzasoleiman, A. Badanidiyuru, A. Karbasi, J. Vondrák, and A. Krause, "Lazier than lazy greedy," in *AAAI Conference on Artificial Intelligence*, 2015, pp. 1812–1818.
- [28] A. V. Sathanur, "Scaling submodular optimization approaches for control applications in networked systems," *arXiv preprint arXiv:1810.02837*, 2018.
- [29] Y. Zhao and P. Vela, "Good graph source code," https://github.com/ivalab/gf_orb_slam2, 2020.
- [30] Y. Zhao and P. Vela, "Good graph raw experimental data," https://github.com/ivalab/FullResults_GoodGraph, 2020.
- [31] S. Leutenegger, S. Lynen, M. Bosse, R. Siegwart, and P. Furgale, "Keyframe-based visual-inertial odometry using nonlinear optimization," *The International Journal of Robotics Research*, vol. 34, no. 3, pp. 314–334, 2015.
- [32] Y. Zhao, W. Ye, and P. Vela, "Low-latency visual SLAM with appearance-enhanced local map building," in *IEEE International Conference on Robotics and Automation*, 2019, pp. 8213–8219.
- [33] G. Sibley, C. Mei, I. Reid, and P. Newman, "Vast-scale outdoor navigation using adaptive relative bundle adjustment," *The International Journal of Robotics Research*, vol. 29, no. 8, pp. 958–980, 2010.
- [34] C. Chou, D. Wang, D. Song, and T. A. Davis, "On the tunable sparse graph solver for pose graph optimization in visual SLAM problems," in *IEEE/RSJ International Conference on Intelligent Robots and Systems*, 2019, pp. 1300–1306.
- [35] L. Carlone, P. F. Alcantarilla, H.-P. Chiu, Z. Kira, and F. Dellaert, "Mining structure fragments for smart bundle adjustment," in *Proceedings of the British Machine Vision Conference*, 2014.
- [36] Y. Litman, Y. Wang, and J. Liu, "Accelerated visual inertial navigation via fragmented structure updates," in *IEEE/RSJ International Conference on Intelligent Robots and Systems*, 2019, pp. 5358–5363.
- [37] M. Kaess, A. Ranganathan, and F. Dellaert, "iSAM: Incremental smoothing and mapping," *IEEE Transactions on Robotics*, vol. 24, no. 6, pp. 1365–1378, 2008.
- [38] M. Kaess, H. Johannsson, R. Roberts, V. Ila, J. J. Leonard, and F. Dellaert, "iSAM2: Incremental smoothing and mapping using the bayes tree," *International Journal of Robotics Research*, vol. 31, pp. 217–236, 2012.
- [39] L. Polok, V. Ila, M. Solony, P. Smrz, and P. Zemcik, "Incremental block Cholesky factorization for nonlinear least squares in robotics," in *Robotics: Science and Systems*, 2013, pp. 328–336.
- [40] V. Ila, L. Polok, M. Solony, and K. Istenic, "Fast incremental bundle adjustment with covariance recovery," in *IEEE International Conference on 3D Vision*, 2017, pp. 175–184.
- [41] M. Shamaiah, S. Banerjee, and H. Vikalo, "Greedy sensor selection: Leveraging submodularity," in *IEEE Conference on Decision and Control*, 2010, pp. 2572–2577.
- [42] S. T. Jawaid and S. L. Smith, "Submodularity and greedy algorithms in sensor scheduling for linear dynamical systems," *Automatica*, vol. 61, pp. 282–288, 2015.
- [43] G. Zhang and P. A. Vela, "Good features to track for visual SLAM," in *IEEE Conference on Computer Vision and Pattern Recognition*, 2015, pp. 1373–1382.
- [44] Y. Zhao and P. Vela, "Good feature selection for least squares pose optimization in VO/VSLAM," in *IEEE/RSJ International Conference on Intelligent Robots and Systems*, 2018, pp. 3569–3574.
- [45] L. Carlone and S. Karaman, "Attention and anticipation in fast visual-inertial navigation," *IEEE Transactions on Robotics*, vol. 35, no. 1, pp. 1–20, 2019.
- [46] K. Khosoussi, M. Giamou, G. S. Sukhatme, S. Huang, G. Dissanayake, and J. P. How, "Reliable graphs for SLAM," *The International Journal of Robotics Research*, vol. 38, no. 2-3, pp. 260–298, 2019.
- [47] F. Dellaert, M. Kaess *et al.*, "Factor graphs for robot perception," *Foundations and Trends in Robotics*, vol. 6, no. 1-2, pp. 1–139, 2017.
- [48] G. L. Nemhauser, L. A. Wolsey, and M. L. Fisher, "An analysis of approximations for maximizing submodular set functions-I," *Mathematical Programming*, vol. 14, no. 1, pp. 265–294, 1978.
- [49] U. Feige, "A threshold of $\ln n$ for approximating set cover," *Journal of the ACM*, vol. 45, no. 4, pp. 634–652, 1998.
- [50] A. Hassidim and Y. Singer, "Robust guarantees of stochastic greedy algorithms," in *International Conference on Machine Learning*, 2017, pp. 1424–1432.
- [51] M. A. Osborne, "Bayesian Gaussian processes for sequential prediction, optimisation and quadrature," Ph.D. dissertation, Oxford University, UK, 2010.
- [52] J. Sola, "Quaternion kinematics for the error-state Kalman filter," *arXiv preprint arXiv:1711.02508*, 2017.
- [53] V. Ila, L. Polok, M. Solony, and P. Svoboda, "SLAM++ a highly efficient and temporally scalable incremental SLAM framework," *The International Journal of Robotics Research*, vol. 36, no. 2, pp. 210–230, 2017.
- [54] R. Kümmerle, G. Grisetti, H. Strasdat, K. Konolige, and W. Burgard, "g2o: A general framework for graph optimization," in *IEEE International Conference on Robotics and Automation*, 2011, pp. 3607–3613.
- [55] R. Mur-Artal, J. M. M. Montiel, and J. D. Tardós, "ORB-SLAM: a versatile and accurate monocular SLAM system," *IEEE Transactions on Robotics*, vol. 31, no. 5, pp. 1147–1163, 2015.
- [56] B. Bodin, H. Wagstaff, S. Saecdi, L. Nardi, E. Vespa, J. Mawer, A. Nisbet, M. Luján, S. Furber, A. J. Davison *et al.*, "SLAMBench2: Multi-objective head-to-head benchmarking for visual SLAM," in *IEEE International Conference on Robotics and Automation*, 2018, pp. 1–8.
- [57] Y. Zhao, J. S. Smith, S. H. Karumanchi, and P. A. Vela, "Closed-loop benchmarking of stereo visual-inertial SLAM systems: Understanding the impact of drift and latency on tracking accuracy," *IEEE Conference on Robotics and Automation*, 2020.
- [58] E. Blem, J. Menon, and K. Sankaralingam, "A detailed analysis of contemporary ARM and x86 architectures," *UW-Madison Technical Report*, 2013.
- [59] M. Burri, J. Nikolic, P. Gohl, T. Schneider, J. Rehder, S. Omari, M. W. Achtelik, and R. Siegwart, "The EuRoC micro aerial vehicle datasets," *The International Journal of Robotics Research*, vol. 35, no. 10, pp. 1157–1163, 2016.

- [60] J. Sturm, W. Burgard, and D. Cremers, "Evaluating egomotion and structure-from-motion approaches using the TUM RGB-D benchmark," in *Workshop on Color-Depth Camera Fusion in Robotics at the IEEE/RJS International Conference on Intelligent Robot Systems*, 2012.
- [61] S. Lynen, M. W. Achtelik, S. Weiss, M. Chli, and R. Siegwart, "A robust and modular multi-sensor fusion approach applied to MAV navigation," in *IEEE/RSJ International Conference on Intelligent Robots and Systems*, 2013, pp. 3923–3929.
- [62] R. Olfati-Saber, "Near-identity diffeomorphisms and exponential epsi-tracking and epsi-stabilization of first-order nonholonomic SE(2) vehicles," in *IEEE American Control Conference*, vol. 6, 2002, pp. 4690–4695.
- [63] W. Garage, "Turtlebot," *Website: <https://www.turtlebot.com/turtlebot2/>*, pp. 11–25, 2011.
- [64] D. Scaramuzza, M. C. Achtelik, L. Doitsidis, F. Friedrich, E. Kosmatopoulos, A. Martinelli, M. W. Achtelik, M. Chli, S. Chatzichristofis, L. Kneip *et al.*, "Vision-controlled micro flying robots: from system design to autonomous navigation and mapping in GPS-denied environments," *IEEE Robotics & Automation Magazine*, vol. 21, no. 3, pp. 26–40, 2014.
- [65] M. Burri, H. Oleynikova, M. W. Achtelik, and R. Siegwart, "Real-time visual-inertial mapping, re-localization and planning onboard MAVs in unknown environments," in *IEEE/RSJ International Conference on Intelligent Robots and Systems*, 2015, pp. 1872–1878.
- [66] S. Paschall and J. Rose, "Fast, lightweight autonomy through an unknown cluttered environment," in *IEEE Aerospace Conference*, 2017, pp. 1–8.
- [67] I. Cvišić, J. Česić, I. Marković, and I. Petrović, "Soft-SLAM: Computationally efficient stereo visual simultaneous localization and mapping for autonomous unmanned aerial vehicles," *Journal of Field Robotics*, vol. 35, no. 4, pp. 578–595, 2018.
- [68] Y. Lin, F. Gao, T. Qin, W. Gao, T. Liu, W. Wu, Z. Yang, and S. Shen, "Autonomous aerial navigation using monocular visual-inertial fusion," *Journal of Field Robotics*, vol. 35, no. 1, pp. 23–51, 2018.
- [69] H. Oleynikova, C. Lanegger, Z. Taylor, M. Pantic, A. Millane, R. Siegwart, and J. Nieto, "An open-source system for vision-based micro-aerial vehicle mapping, planning, and flight in cluttered environments," *Journal of Field Robotics*, vol. 37, no. 4, pp. 642–666, 2020.



Patricio A. Vela is an associate professor in the School of Electrical and Computer Engineering, and the Institute of Robotics and Intelligent Machines, at Georgia Institute of Technology, USA. His research interests lie in the geometric perspectives to control theory and computer vision. Recently, he has been interested in the role that computer vision can play for achieving control-theoretic objectives of (semi-)autonomous systems. His research also covers control of nonlinear systems, typically robotic systems.

Prof. Vela earned his B.Sc. degree in 1998 and his Ph.D. degree in control and dynamical systems in 2003, both from the California Institute of Technology, where he did his graduate research on geometric nonlinear control and robotics. In 2004, Dr. Vela was as a post-doctoral researcher on computer vision with School of ECE, Georgia Tech. He join the ECE faculty at Georgia Tech in 2005.

Prof. Vela is a member of IEEE.



Yipu Zhao is a Research Scientist at Facebook Reality Lab (FRL). Prior to joining FRL, he obtained his Ph.D. in 2019, under the supervision of Patricio A. Vela, at the School of Electrical and Computer Engineering, Georgia Institute of Technology, USA. Previously he received his B.Sc. degree in 2010 and M.Sc. degree in 2013, at the Institute of Artificial Intelligence, Peking University, China. His research interests include visual odometry/SLAM, 3D reconstruction, and multi-object tracking.

Dr. Zhao is a member of IEEE.



Justin S. Smith is a Ph.D. candidate in the School of Electrical and Computer Engineering, at the Georgia Institute of Technology. His research focuses on utilizing perception space and deep learning to improve robot navigation performance, especially when under computational resource limit. Previously, he earned his B.Sc in Electrical Engineering from Brigham Young University (2012).

Justin S. Smith is a student member of IEEE.